공학박사 학위논문

Engineering Strategy for Robust Stability of All-Inorganic Black $CsPbI_3$ Perovskites

흑색 상 무기 $CsPbI_3$ 페로브스카이트의 장기 안정성 향상 공정개발에 관한 연구

2020년 8월

서울대학교 융합과학기술대학원

융합과학부 나노융합전공

조 남 광

Engineering Strategy for Robust Stability of All-Inorganic Black $CsPbI_3$ Perovskites

지도교수 김 연 상

이 논문을 공학박사학위 논문으로 제출함.

2020년 7 월

서울대학교 융합과학기술대학원
융합과학부 나노융합전공

조 남 광

조남광의 박사학위 논문을 인준함

2020 년 6 월

위 원 장	박 원 철	인
부위원장	김 연 상	인
위 원	이 강 원	인
위 원	강 성 준	인
위 원	배 완 기	인

Abstract

Engineering Strategy for Robust Stability of All-Inorganic Black $CsPbI_3$ Perovskites

Nam-Kwang Cho

Program in Nano Science and Technology

The Graduate School of Convergence Science & Technology

Seoul National University

The halide perovskite with an adjustable direct bandgap, high absorption coefficient, and long exciton diffusion length has attracted considerable attention in the field of solar cell and photodetector as the next generation light absorber. Recently, researches have been intensively conducted to secure structural long-term stability under ambient conditions of a black colored (α, γ phase) halide perovskite with low-bandgap (~1.72 eV), which has excellent absorption property along the entire visible light region. However, there is still a challenge to further methodological improvement of the perovskite long-term stability issue.

In this thesis, two engineering strategies for securing long-term stability of black phase perovskite under atmospheric conditions were proposed sequentially, and photoelectric properties were evaluated by applying them to phototransistor and photoresistor devices respectively. Firstly, I introduced the implementation of all-inorganic α-$CsPbI_xBr_{3-x}$, one of the partial substitution methods, that secured long-term stability under atmospheric conditions by introducing the multi anion strategy with low temperature process. Additionally, phototransistors were fabricated through the heterojunction of $CsPbI_xBr_{3-x}$ and IGZO oxide semiconductor, and the characteristics of the phototransistor were evaluated. Throughout this study, I also found that the $CsPbI_xBr_{3-x}$/IGZO heterojunction significantly cushions the photoillumination stress of IGZO

Furthermore, I suggest a robust strategy to ensure the structural, electrical long-term stability of γ-$CsPbI_3$ under ambient conditions through the ultraviolet (UV) curable oligo(ethylene glycol) dimethacrylate (OEGDMA). Oxygen lone pair electrons of the OEGDMA capture Cs^+ and Pb^{2+} cations, improving the crystal growth of γ-$CsPbI_3$ around OEGDMA. Additionally, polymer network of OEGDMA processed by UV irradiation, strongly contributes to maintaining the black phase of γ-$CsPbI_3$ structure tight for more than 35 days in ambient conditions. X-ray photoelectron spectroscopy (XPS) and X-ray diffraction (XRD) analysis were performed to understand the effect of UV-cured polymer network of OEGDMA which is introduced for maintaining the black phase of γ-$CsPbI_3$. In order to

evaluate the optoelectronic properties, two-terminal photoresistors were fabricated in the lateral direction and the effective photocurrent under the visible light was confirmed. The optimized UV-cured 3 wt% OEGDMA/γ-$CsPbI_3$ perovskite film showed that ~90% of the initial electrical properties responding to red, green, and blue light were maintained even after 35 days. These results provide that introducing the photocurable polymer network is an innovative strategy that can effectively contribute to the long-term stability of the halide perovskite.

Keywords: Long-Term Stability, γ-$CsPbI_3$, Inorganic Halide Perovskite, Black Phase, UV-Curable Polymer Network, Photoresistor

Student Number: 2015-30720

Contents

List of figures and tables

bandgap of the $CsPbI_xBr_{3-x}$ perovskite films fabricated with different concentrations of additive $CsBr/PbBr_2$ (0 wt%, 5 wt%, 12 wt%, and 21 wt%) in the $CsPbI_3$ precursor solution.

Figure 3. 3 (a) Photographs and (b) UV-vis absorption of $CsPbI_xBr_{3-x}$ perovskite films fabricated with different concentrations of additive $CsBr/PbBr_2$ (5 wt%, 12 wt%, 21 wt%) in the $CsPbI_3$ precursor solution for 1 month, showing phase transition under ambient conditions (20 °C, 25% RH). (c) XRD patterns of the $CsPbI_xBr_{3-x}$ film fabricated with additive 12 wt%-$CsBr/PbBr_2$ in the $CsPbI_3$ precursor solution, measured when just formed and after 1 month.

Figure 3. 4 The schematic of the device structures. (a) double-layered heterojunction phototransistor with perovskite/IGZO. (b) conventional IGZO phototransistor. (c) single-layered $CsPbI_2Br$ perovskite phototransistor.

Figure 3. 5 FESEM cross section image of the heterojunction film with $CsPbI_2Br$ and IGZO.

Figure 3. 6 Transfer characteristics of (a) conventional IGZO phototransistor, (b) single-layered $CsPbI_2Br$ (additive 12 wt%-$CsBr/PbBr_2$ in the $CsPbI_3$ precursor solution) perovskite phototransistor, (c) heterojunction phototransistor with intrinsic $CsPbI_3$ (additive 0 wt%-$CsBr/PbBr_2$ in the $CsPbI_3$ precursor solution)/IGZO, and (d) heterojunction phototransistor with $CsPbI_2Br$ (additive 12

wt%-CsBr/$PbBr_2$ in the $CsPbI_3$ precursor solution)/IGZO at various wavelengths of light illumination (dark, 450 nm, 532 nm and 635 nm) at V_{DS} = 1 V. Schematic diagrams of the current flows based on an energy band diagram in heterojunction with $CsPbI_2Br$/IGZO phototransistor channel at (e) $V_g < V_{th}$ and (f) $V_g > V_{th}$ under the visible light illumination.

Figure 3. 7 Transfer characteristics of heterojunction phototransistors with $CsPbI_xBr_{3-x}$ / IGZO under dark and light irradiation (450 nm, 532 nm, and 635 nm wavelength of 1 mW/cm^2 power density) at V_{DS} = 1 V, which perovskite films were fabricated with the different concentration of additives (a) 5 wt%-, (b) 12 wt%-, and (c) 21 wt%-CsBr/$PbBr_2$ in the $CsPbI_3$ precursor solution.

Figure 3. 8 Bandgap of the (a) $CsPbI_2Br$ and (b) IGZO by absorption peak. Work function of (c) $CsPbI_2Br$ and (d) IGZO by UPS. (e) Energy band diagram of heterojunction with $CsPbI_2Br$ / IGZO.

Figure 3. 9 (a) Responsivity and (b) Detectivity of heterojunction phototransistor with CsPbI2Br (additive 12 wt%-PbBr/$CsBr_2$ in the $CsPbI_3$ precursor solution) / IGZO under the 635 nm light illumination (power density = 1 mW/cm^2) at VDS = 1 V.

Figure 3. 10 (a) Responsivity and detectivity of the heterojunction phototransistor with $CsPbI_2Br$ (additive 12 wt%-PbBr/$CsBr_2$ in the $CsPbI_3$ precursor

solution)/IGZO at various wavelengths of light illumination (dark, 450 nm, 532 nm and 635 nm) at V_{DS} = 1 V. (b) Transfer characteristics of the heterojunction phototransistor with $CsPbI_2Br$/IGZO under different incident light intensities at 635 nm (V_{DS} = 1 V). (c) Transient response of the heterojunction phototransistor with $CsPbI_2Br$/IGZO under 450 nm, 532 nm and 635 nm pulse light at a constant V_g = 5 V, V_{ds} = 1 V. (d) Enlarged 1 cycle figure of the transient response of the heterojunction phototransistor under 450 nm, 532 nm and 635 nm pulse light. (e) I_{ds} measurements of the heterojunction phototransistor with $CsPbI_2Br$/IGZO and the heterojunction phototransistor with intrinsic $CsPbI_3$/IGZO for 1 month under ambient conditions (20 °C, 25% RH).

Figure 3. 11 (a) Transient response of conventional IGZO phototransistor under 450 nm pulse light at a constant V_g =-5 V, V_{ds} = 1 V. (b) Enlarged 1 cycle figure of the transient response of conventional IGZO phototransistor under 450 nm pulse light.

Figure 4. 1 Feasibility of long-term stable perovskite by UV-curable polymer network. a, b, The UV-vis spectrum of the reference CsPbI3, and CsPbI3 with or without UV-curing after the addition of OEGDMA, at the fresh state (a), and after 5 days left in the ambient conditions (b). c, d, Tauc's plot derived from the UV-vis spectroscopy analysis data of the fresh state (c), and after 5 days left in the ambient

conditions (d). Inset: photographic images of the reference CsPbI3, and CsPbI3 with or without UV-curing after the addition of OEGDMA.

Figure 4. 2 ATR-FTIR spectroscopy analysis to investigate qualitatively for the conversion of C=C double bonds in the methacrylate group of OEGDMA whether UV irradiation.

Figure 4. 3 UV-curing reaction mechanism of the OEGDMA. Each OEGDMA has two methacrylate end groups, which, when exposed with UV, react with four other methacrylate groups through radical polymerization to make a covalent bond, and the OEGDMA forms a cross-linked network.

Figure 4. 4 XRD patterns of the reference $CsPbI_3$, and $CsPbI_3$ with or without UV-curing after the addition of OEGDMA, at the fresh state (a), and after 7 days left in the ambient conditions (b). Asterisk: $HPbI_{3+x}$ [20]

Figure 4. 5 A conceivable mechanism for the introduction of the OEGDMA UV-curing strategy to improve the long-term stability of $CsPbI_3$. a, Step 1: Induced $CsPbI_3$ nuclei formation and crystal growth from the OEGDMA molecular backbone chain by the OEGDMA's oxygen lone pair electrons in the precursor solution. b, Step 2: UV-curing process immediately before cooling, on the spin-coated and annealed $CsPbI_3$ after the addition of OEGDMA. UV irradiation: 365nm, 400 $mW \cdot cm^{-2}$ for 5 seconds. c, Step 3: Establishment of the robust γ-$CspbI_3$ with

the UV-cured OEGDMA polymer network.

Figure 4. 6 DLS analysis for $CsPbI_3$ precursor solution containing with different amounts of OEGDMA (0, 0.5, 1, 3, 5 wt%).

Figure 4. 7 a-e, Accumulated UV-vis absorbance spectra while exposing γ-$CsPbI_3$ (0, 0.5, 1, 3, and 5 wt% OEGDMA) to the ambient conditions for 35 days.

Figure 4. 8 Ambient conditions where γ-$CsPbI_3$ (0, 0.5, 1, 3, and 5 wt% OEGDMA) stored for 35 days. The ambient conditions measured with 20.50 ± 1.10 °C for temperature and 26.81 ± 2.56 % for relative humidity, respectively for 35 days.

Figure 4. 9 A linear relationship with the OEGDMA content and the γ-$CsPbI_3$ (0, 0.5, 1, 3, and 5 wt% OEGDMA) absorbance peak intensity at the 720nm position.

Figure 4. 10 FE-SEM top view images of γ-$CsPbI_3$ (0, 0.5, 1, 3, and 5 wt% OEGDMA). Scale bar: 2 ㎛.

Figure 4. 11 Time-dependent photographic results obtained by observing the optical color change of the γ-$CsPbI_3$ (0, 0.5, 1, 3, and 5 wt% OEGDMA) thin films during 35 days in ambient conditions. The red square box represents the limitation of γ-phase stability that begins to transition from the γ-phase to the δ-phase.

Figure 4. 12 XPS analysis on the fresh γ-$CsPbI_3$ (0, 0.5, 1, 3, and 5 wt% OEGDMA) at full range (a), Pb 4f (b), I 3d (c), and Cs 3d (d).

Figure 4. 13 a-e, Photoresponse I-V characteristics of photoresistors including fresh

γ-$CsPbI_3$ (0, 0.5, 1, 3, and 5 wt% OEGDMA), under irradiation of 0.4 mW ·cm^{-2} of red (635 nm), green (532 nm), and blue (450 nm) LED light sources.

Figure 4. 14 a-e, Photoresponse I-V characteristics of photoresistors including 35 days elapsed γ-$CsPbI_3$ (0, 0.5, 1, 3, and 5 wt% OEGDMA), under irradiation of 0.4 mW ·cm^{-2} of red (635 nm), green (532 nm), and blue (450 nm) LED light sources.

Figure 4. 15 The comparison of additional optical response parameters between as-prepared (a) and after 35 days (b) of Au/γ-$CsPbI_3$ (0, 0.5, 1, 3, and 5 wt% OEGDMA)/Au photoresistors. Unit of the parameters: *EQE* (%), J_{photo}/J_{dark}, *R* (A/W), *D** (Jones).

Figure 4. 16 Photocurrent–time responses of the reference γ-$CsPbI_3$ photoresistor at fresh state (a) and after 35 days (b). Photocurrent–time responses of the γ-$CsPbI_3$ (3 wt% OEGDMA) photoresistor at fresh state (d) and after 35 days (e). Photocurrent–time response was measured at 40 V applied bias in the dark and under illumination using the LEDs at 635 nm, 532nm, 450nm with fixed light intensity (P_{in} = 0.4 mW ·cm^{-2}) and frequency (1 Hz).

Figure 4. 17 The transient response time of the γ-$CsPbI_3$ (3 wt% OEGDMA) photoresistor at fresh state (a) and after 35 days (b). The transient response time was measured at the 10th period during the 2 Hz, 50% duty cycle with fixed light intensity (P_{in} = 0.4 mW ·cm^{-2}).

Chapter 1 Introduction

1.1 Overview

The halide perovskite with an adjustable direct bandgap, high absorption coefficient, and long exciton diffusion length has attracted considerable attention in the field of solar cell and photodetector as the next generation light absorber [1-3]. Recently, researches have been intensively conducted to secure structural long-term stability under ambient conditions of a black colored (α, γ phase) halide perovskite with low-bandgap (~1.72 eV), which has excellent absorption property along the entire visible light region. Among them, organic-inorganic hybrid perovskites in which organic cations such as methylammonium or formamidinium are applied to the position A of ABX_3 structure have been preferentially studied for realizing a cubic structure by satisfying the Goldschmidt tolerance factor ($0.81<t<1.1$, $t = (r_A + r_X)/\sqrt{2}(r_B + r_X)$, where r_A, r_B, and r_X are the ionic sizes of A, B, and X, respectively) [4, 5]. However, due to the inherent volatility problems of the organic cations, all-inorganic perovskite ($CsPbX_3$, X = I, Br, Cl) which replaced the organic cation with cesium is drawing attention recently [6-11]

Particularly, in the case of $CsPbI_3$ in which the iodine is in the X position, it is intensively studied as a visible light detection material because it can effectively

absorb the entire visible light. However, there is still a challenge to further methodological improvement of the perovskite long-term stability issue.

In this thesis, two engineering strategies for securing long-term stability of black phase perovskite under atmospheric conditions were proposed sequentially, and photoelectric properties were evaluated by applying them to phototransistor and photoresistor devices respectively. In Chapter 2, the fundamental knowledges of perovskite structures and the characteristics of the photodetectors are introduced. Chapter 3 introduced the implementation of all-inorganic α -$CsPbI_xBr_{3-x}$, one of the partial substitution methods, that secured long-term stability under atmospheric conditions by introducing the multi anion strategy with low temperature process [12]. Additionally, phototransistors were fabricated through the heterojunction of $CsPbI_xBr_{3-x}$ and IGZO oxide semiconductor, and the characteristics of the phototransistor were evaluated. Throughout this study, I also found that the $CsPbI_xBr_{3-x}$ /IGZO heterojunction significantly cushions the photoillumination stress of IGZO [13].

Furthermore, in Chapter 4, I suggest a robust strategy to ensure the structural, electrical long-term stability of γ-$CsPbI_3$ under ambient conditions through the ultraviolet (UV) curable oligo(ethylene glycol) dimethacrylate (OEGDMA) that overcome the bandgap widening issue of partial substitution method. Oxygen lone

pair electrons of the OEGDMA capture Cs^{+} and Pb^{2+} cations, improving the crystal growth of γ-$CsPbI_3$ around OEGDMA. Additionally, polymer network of OEGDMA processed by UV irradiation, strongly contributes to maintaining the black phase of γ-$CsPbI_3$ structure tight for more than 35 days in ambient conditions. In order to evaluate the optoelectronic properties, two-terminal photoresistors were fabricated in the lateral direction and the effective photocurrent under the visible light was confirmed. The optimized UV-cured 3 wt% OEGDMA /γ-$CsPbI_3$ perovskite film showed that ~90% of the initial electrical properties responding to red, green, and blue light were maintained even after 35 days. These results provide that introducing the photocurable polymer network is an innovative strategy that can effectively contribute to the long-term stability of the halide perovskite.

1.2 References

[1] Park, N. -K. Organometal perovskite light absorbers toward a 20% efficiency low-cost solid-state mesoscopic solar cell. J. Phys. Chem. Lett. 4, 2423−2429 (2013).

[2] Xing, G. & Nripan, M. et al. Long-range balanced electron and hole-transport lengths in organic-inorganic $CH_3NH_3PbI_3$. *Science* **342**, 344-347 (2013).

[3] Gao, P. et al. Organohalide lead perovskites for photovoltaic applications. Energy *Environ. Sci.* **7**, 2448-2463 (2014).

[4] Xu, L. et al. A comprehensive review of doping in perovskite nanocrystals/quantum dots: evolution of structure, electronics, optics, and light-emitting diodes. *Materials today. Nano* **6**, 100036 (2019).

[5] Bhalla, A. S. et al. The perovskite structure—a review of its role in ceramic science and technology. *Mater. Res. Innov.* **4**, 3-26 (2000).

[6] Nam, J. K. et al. Methodologies toward efficient and stable cesium lead halide perovskite-based solar cells. *Adv. Sci.* 1800509 (2018).

[7] Hoffman, J. B. et al. $CsPbBr_3$ solar cells: controlled film growth through layer-by-layer quantum dot deposition. *Chem. Mater.* **29**, 9767−9774 (2017).

[8] Travis, W. et al. On the application of the tolerance factor to inorganic and hybrid halide perovskites: a revised system. *Chem. Sci.* **7**, 4548-4556 (2016).

[9] Sutton, R. J. et al. Bandgap-tunable cesium lead halide perovskites with high thermal stability for efficient solar cells. *Adv. Energy Mater.* **6**, 1502458 (2016).

[10] Liang, J. et al. All-inorganic perovskite solar cells. *J. Am. Chem. Soc.* **138**, 15829−15832 (2016).

[11] Chen, H. et al. Inorganic perovskite solar cells: A rapidly growing field. *Sol. RRL* **2**, 1700188 (2018).

[12] Na, H. -J. et al. A visible light detector based on a heterojunction phototransistor with a highly stable inorganic $CsPbI_xBr_{3-x}$ perovskite and In–Ga–Zn–O semiconductor double-layer. *J. Mater. Chem.* C **7**, 14223-14231 (2019)

[13] Jeon, S. et al. Gated three-terminal device architecture to eliminate persistent photoconductivity in oxide semiconductor photosensor arrays. *Nat. Mater.* 11, 301-305 (23012)

Chapter 2 Fundamental and Literature Review

2.1 Goldschmidt tolerance factor

The perovskite structure can be determined by compounds of formula ABX_3, where A and B are cations and X is an anion (Fig. 2. 1). It is based on a cubic array of corner sharing BX_6 octahedra, with the A site cation located within the corner edge cavities. For the perovskite structure, the most commonly used and most successful geometric ratio is the Goldschmidt tolerance factor, *t*, defined as follows [1]:

$$t = \frac{r_A + r_X}{\sqrt{2}(r_B + r_X)} \tag{2.1}$$

where r_A and r_B are the ionic radius of the A and B site cationsrespectively, and r_X is the ionic radius of the anion. The tolerance factor determines whether the A site cation can locate within the cavities in the BX_3 framework. A tolerance factor of 1 indicates a perfect cubic; in the range $0.8 \leq t \leq 1$ perovskites generally do form the cubic phase, although in the lower part of this range they may be distorted due to tilting of the BX_6 octahedra and lowering of the symmetry. If $t > 1$, this means the A site cation is too large and generally hinders formation of a perovskite, and if $t <$

0.8, the A cation is too small, the perovskite structure is not accomplished. the *t*-values of different A-site cation in $APbX_3$ are marked in Table 2. 1 according to eq. 2. 1. It seems that size of organic MA^+ and FA^+ are relatively ideal candidates for the cubic perovskite structure, while Cs^+ are slightly small to be perfect A-site candidate [2]. However, MA^+ and FA^+ based perovskite structure suffer from the unsatisfactory thermalstability for the organic components [3, 4]. To solve the problem, all-inorganic perovskite have been developed by introducing inorganic cation Cs^+ with various engineering technique.

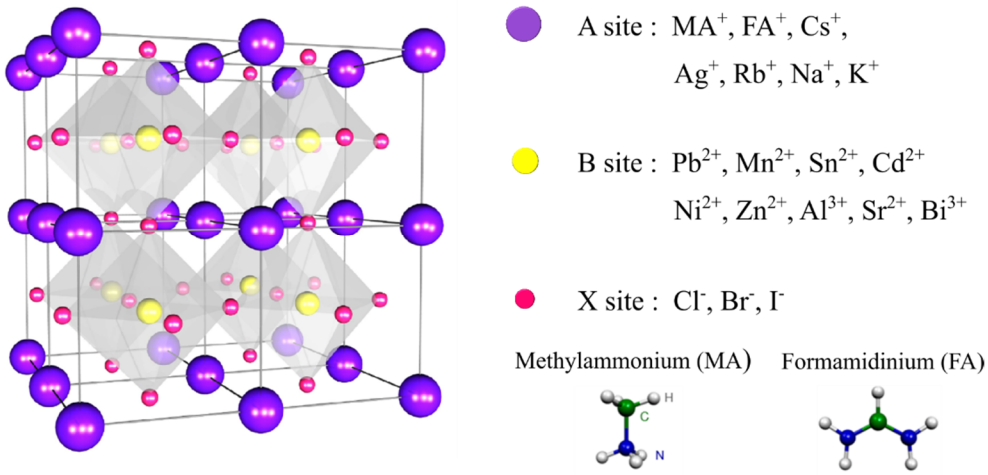

Figure 2. 1 Schematic diagram of ABX_3 perovskite structure and the candidates for each position.

A-cation	Ionic radius (pm)	Tolerance factor for $APbI_3$
Li	76	0.62
Na	102	0.67
K	138	0.75
Rb	152	0.78
Cs	1.67	0.81
MA	217	0.91
FA	253	0.99

Table 2. 1 Tolerance factors calculated for each A cation candidate in $APbI_3$ composition.

2.2 Octahedron factor

Besides tolerance factor *t*, the octahedral factor μ, which is additional semiempirical geometric parameter, is used to evaluate the octahedral stability. μ can be described as follows [5]:

$$\mu = \frac{r_B}{r_X} \tag{2. 2}$$

The range of μ between 0.442 and 0.895 would be beneficial for the stable $[BX_6]^{4-}$ octahedral form. The μ values of B-site related octahedron varying with different cations are shown in Fig. 2. 2. The choice of B-site cation not only has to satisfy the range of tolerance factor *t*, but also needs to satisfy the requirements of octahedral factor μ. Although a fair amount of efforts has been made to explore the substitution of Pb, few altanative B-site cations are available for halide perovskite structures. Apart from the structure stability, the luminescence characteristics and electronic structurechange a lot owing to the alteration of B-site cations.

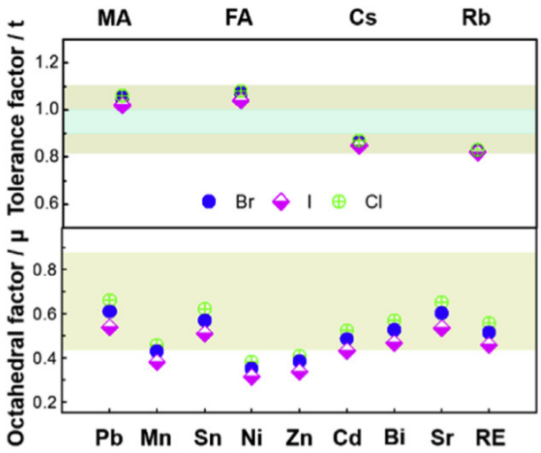

Figure 2. 2 The tolerance factor of lead halide perovskite with different A-site cations and X-site anions, and octahedral factor of $[BX_6]^{4-}$ coodination varying with B-site cations and X-site anions.

2.3 Four phases of perovskite via temperature changes

Regarding phase stability, single-cation $CsPbI_3$ systems form a thermodynamically stable yellow δ-phase (non-perovskite) before undergoing reversible high-temperature phase transitions to their optically active black perovskite phases; α (cubic), β (tetragonal) and γ (orthorhombic). The thermal phase relations for $CsPbI_3$ is depicted in Fig. 2. 3, with the relative transitions shown in Fig. 2. 4. The term "black" is used to define collectively the (pseudo-)cubic phases, as they typically exhibit similar optoelectronic properties. At room temperature, the black phase is unstable [6]. As seen in Fig. 2. 3, the black α-$CsPbI_3$ perovskite can, depending on conditions, pass through a variety of different restructuring paths. The thermodynamically preferred cooling path (path 2) [7] is mediated by the series of structural distortions (Fig. 2. 4). When the requisite sample preparation and cooling rates are used, a black phase at the room temperature can persist (paths 3 and 4 in Fig. 2. 3) in the form of a pseudo-cubic phase. A metastable black phase will only maintain at room temperature when the strong driving force to transform into the yellow phase (path 5) is successfully countered. For example, upon mild reheating (60 - 100°C), the metastable black phase (path 6) will normally turn yellow [6] once its saddle point is energetically overcome. Thus, the problem is how to form a stable black $CsPbI_3$ perovskite for room temperature device operation.

Recent studies offer a range of solutions, each following at least one of three general approaches: (i) forming nanocrystals [8, 9], (ii) surface functionalization [10], and (iii) compositional tuning [11]. Interestingly, when forming of a perovskite-substrate heterojunction in thin-film device architectures, tensile strain was recently shown to manifest at room temperature because of the large mismatch in thermal expansion coefficients (α_T) of the perovskite layer (~50×10^{-6} K^{-1} for lead iodide-based perovskites) and typical transparent substrates (both ITO and glass reside between 4×10^{-6} to 9×10^{-6} K^{-1}). By definition, strain will push the competing perovskite phases into a relative state of thermodynamic unequilibrium [12]. Within this context, strain engineering can favor formation of a desired phase or can even lead to new phases. For example, the strain introduced into $CsPbI_3$ nanocrystals processed with hydroiodic acid [13] has been connected to improved stability.

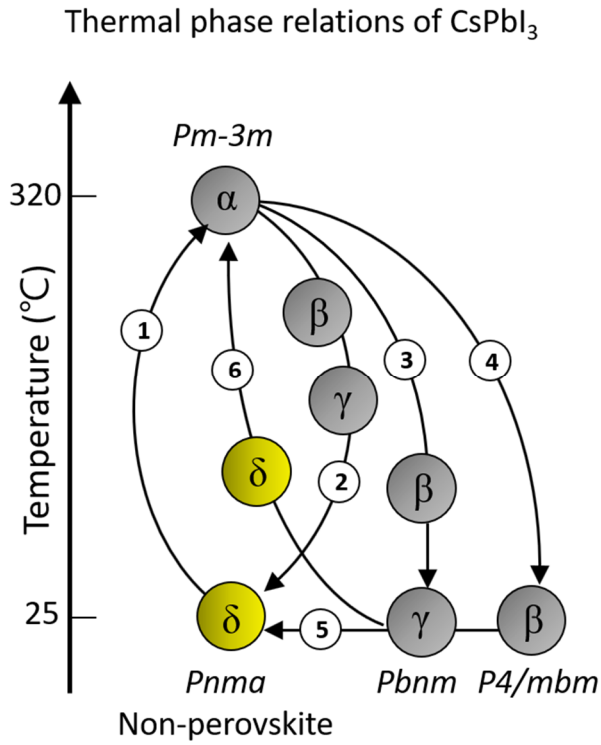

Figure 2. 3 Thermal phase relations of $CsPbI_3$.

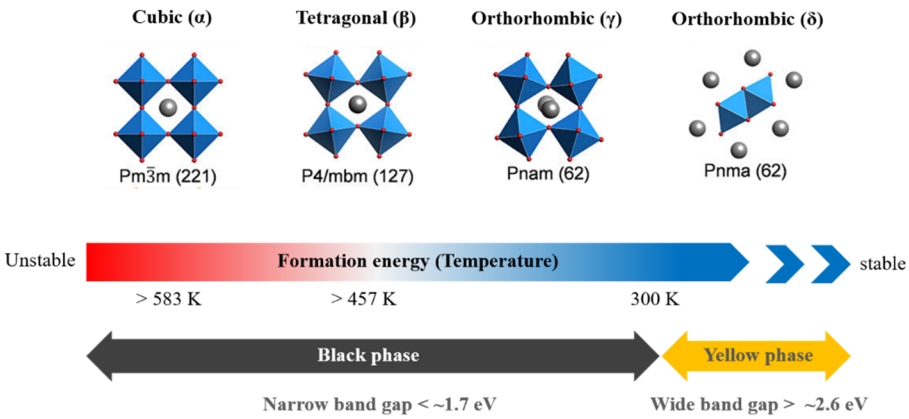

Figure 2. 4 Crystal structure of the different phases and their relative phase transitions according to the temperature.

2.4 References

[1] Travis, W. and Clover, E. N. K. et al. On the application of the tolerance factor to inorganic and hybrid halide perovskites: a revised system. *Chem. Sci.* **7**, 4548-4556 (2016).

[2] Filip, M. R. et al. Steric engineering of metal-halide perovskites with tunable optical band gaps. *Nat. Commun.* **5**, 5757 (2014).

[3] Singh, S. and Kabra, D. Influence of solvent additive on the chemical and electronic environment of wide bandgap perovskite thin films. *J. Mater. Chem. C* **6**, 12052-12061 (2018).

[4] Yantara, N. et al. Inorganic halide perovskites for efficient light-emitting diodes. *J. Phys. Chem. Lett.* **6**, 4360–4364 (2015).

[5] Xu, L. et al. A comprehensive review of doping in perovskite nanocrystals/quantum dots: evolution of structure, electronics, optics, and light-emitting diodes. *Materials today. Nano* **6**, 100036 (2019).

[6] Dastidar, S. et al. Quantitative phase-change thermodynamics and metastability of perovskite-phase cesium lead iodide. *J. Phys. Chem. Lett.* **8**, 1278–1282 (2017).

[7] Marronnier, A. et al. Anharmonicity and disorder in the black phases of cesium lead iodide used for stable inorganic perovskite solar cells. *ACS Nano* **12**, 3477–

3486 (2018).

[8] Zhang, D. et al. Ultrathin colloidal cesium lead halide perovskite nanowires. *J. Am. Chem. Soc.* **138**, 13155–13158 (2016)

[9] Swarnkar, A. et al. Quantum dot-induced phase stabilization of α-CsPbI3 perovskite for high-efficiency photovoltaics. *Science* **354**, 92–95 (2016).

[10] Fu, Y. et al. Stabilization of the metastable lead iodide perovskite phase via surface functionalization. *Nano Lett.* **17**, 4405–4414 (2017).

[11] Li, Z. et al. Stabilizing perovskite structures by tuning tolerance factor: formation of formamidinium and cesium lead iodide solid-state alloys. *Chem. Mater.* **28**, 284–292 (2016).

[12] Rabe, K. M. et al. Strain coupling in perovskite structural transitions: A first principles approach. *Ferroelectrics* **194**, 119–134 (1997).

[13] Eperon, G. E. et al. Inorganic caesium lead iodide perovskite solar cells. *J. Mater. Chem. A Mater. Energy Sustain.* **3**, 19688–19695 (2015).

Chapter 3 A visible light detector based on a heterojunction phototransistor with a highly stable inorganic $CsPbI_xBr_{3-x}$ perovskite and In–Ga–Zn–O semiconductor double-layer

3.1 Overview

Amorphous In–Ga–Zn–O (IGZO) has been extensively studied as a thin-film transistor [1,2] and an optical sensor [3] in display devices because of its high field-effect carrier mobility, low off-current and transparency in the visible light region [4,5]. However, in optical sensors and image sensing applications, the IGZO photodetector is allowed to be applied only to the ultraviolet (UV) region except for visible and near-infrared light due to the large optical bandgap (3.5 eV) of IGZO [6]. Moreover, because of the persistent photoconductivity (PPC) phenomenon induced by the permanent photoconductive ionized vacancy sites of IGZO [7], the response time of the photodetector increases considerably after the UV light is turned on or off, resulting in poor transient response characteristics. In order to extend the detection range and improve the optoelectronic response characteristics, heterojunction photodetectors with IGZO and various optical absorption layers have been suggested. In these structures, absorption layers such as quantum dots

(CdSe QDs, CdS QDs, and PbS QDs) [8–10] a metal nanoparticle [11] and twodimensional materials (MoS_2 and graphene) [12–15] were covered onto the IGZO film, which generated and transferred the photoinduced charge carriers. Even though these approaches could absorb the wide range of light due to the narrow bandgap of the absorption layers, such absorbers require a complicated procedure to be formed onto IGZO. In addition, the previously reported narrow bandgap materials are hard to deposit uniformly over a large area. Recently, perovskite, referred to as the ABX_3 (where A is the organic or inorganic cation, B is the divalent metal cation and X is the halide anion) structure [16], has been considered as an attractive alternative to optoelectronic absorbers due to its broad optical absorption, low exciton binding energy, charge transport properties and bandgap tunability [17–20]. In particular, film fabrication using a solution process allows uniform integration of solar cells [19, 20], photodiodes [21, 22], photoresistors [23, 24] and phototransistor devices [25, 26] into a hybrid device over a large area. The phototransistors based on the IGZO semiconductor were introduced for the detection of visible light by coating with organic–inorganic hybrid perovskite, methylammonium lead iodide ($MAPbI_3$) [27, 28]. However, the $MAPbI_3$ film undergoes a reversible phase transition at 55 °C and considerably degrades to PbI_3 above 85 °C [29, 30]. In addition, the $MAPbI_3$ film is strongly unstable under

moisture containing atmospheres [31]. By replacing the organic cation with an inorganic Cs cation in perovskite, all-inorganic cesium lead halide ($CsPbI_3$) could exhibit better thermal stability and be more robust to moisture than those of $MAPbI_3$ as well as maintain its electrical and structural properties [32, 33]. To fabricate the cubic phase $CsPbI_3$ (α-$CsPbI_3$) by a solution process, a high temperature (over 300 °C) is necessary because the Cs cation is too small to bind to PbI_6. 34 Generally, the bandgap of α-$CsPbI_3$ fabricated using the high-temperature process is 1.73 eV [35], which absorbs the entire visible light region. However, $CsPbI_3$ produced by annealing below 250 °C is formed in an orthorhombic phase (δ-$CsPbI_3$) rather than α-$CsPbI_3$, which has a large bandgap of 2.82 eV and limits the absorption of the entire visible light region [34]. In order to fabricate the a-phase inorganic perovskite film, hydroiodic acid or chlorobenzene was added into the $CsPbI_3$ precursor solution to induce micro-deformation in the $CsPbI_3$ lattice [19, 36]. Another method of fabricating the α-phase inorganic perovskite film, partially replacing I with the comparatively smaller Br in the $CsPbI_3$ structure was suggested [37]. However, these studies showed that a high processing temperature was still required, which may be a critical limitation for a wide range of applications. Moreover, the inorganic perovskite films produced by these methods showed a short α-phase retention time (under 10 days) after fabrication and still suffered from strong deterioration under

ambient conditions.

In this chapter, I propose a new method of manufacturing an α-phase perovskite, α-$CsPbI_xBr_{3-x}$, using a low-temperature solution process (90 °C annealing) by adding CsBr and $PbBr_2$ in the $CsPbI_3$ precursor solution, which guarantees long-term stability over 1 month under ambient conditions (20 °C, 25% RH). Also, using the α-$CsPbI_xBr_{3-x}$ film, we fabricated an entire visible light detector based on a heterojunction phototransistor consisting of a perovskite/IGZO double-layer which acts as a light absorption layer and a charge transport layer, respectively. The concentration of additives CsBr and $PbBr_2$ in the precursor solution prepared by dissolving CsI and PbI_2 in dimethyl-sulfoxide (DMSO) is optimized to maintain α-$CsPbI_xBr_{3-x}$ by increasing the binding energy of Br and I in the $CsPbI_xBr_{3-x}$ structure. At 12 wt% concentration of additives CsBr and $PbBr_2$ relative to the total molar amount of CsI and PbI_2, most of the Br ions are incorporated into the lattice to form the α-$CsPbI_xBr_{3-x}$ film, which exhibits only a small shift in the bandgap relative to the intrinsic $CsPbI_3$ (0 wt% additives CsBr and $PbBr_2$ in the $CsPbI_3$ precursor solution) film (from 1.73 eV to 1.82 eV), and still absorbs the visible light region considerably. The all-inorganic heterojunction phototransistor with α-$CsPbI_xBr_{3-x}$/ IGZO shows a responsivity of 26.48 A/W, a detectivity of 8.42×10^{14} Jones, and an external quantum efficiency (EQE) of 51% under red light illumination (635 nm),

which exhibits high stability over 1 month under ambient conditions (20 °C, 25% RH). In addition, the response time of the heterojunction phototransistor is considerably faster than that of the conventional IGZO phototransistor degraded by the PPC phenomenon under light illumination [7]. I believe that these results will strongly contribute to expanding the availability of the all-inorganic heterojunction phototransistors with perovskite and oxide semiconductors. Also, these results suggest a new approach for fabricating highly stable optical perovskite materials.

3.2 The correlation between $CsBr/PbBr_2$ content in the $CsPbI_3$ precursor solution and black α-$CsPbI_xBr_{3-x}$ optical long-term stability

In order to produce a highly stable perovskite $CsPbI_xBr_{3-x}$ film using a low-temperature solution process, CsI and PbI_2 with a molar ratio of 1 : 1 were first completely dissolved in 1 ml DMSO to prepare a 0.4 M $CsPbI_3$ precursor solution. And then, to produce $CsPbI_xBr_{3-x}$ films with different ratios of I and Br, the additives CsBr and $PbBr_2$ were added at concentrations from 0 wt% to 21 wt% relative to the 0.4 M $CsPbI_3$ precursor solution, which was stirred at 500 rpm for 24 h. The perovskite precursor solution was spin-coated at 3500 rpm for 45 s using a one-step process and the annealing temperature of the film was maintained at a low temperature of 90 °C for 5 min. Perovskite films are expressed as the $CsPbI_xBr_{3-x}$ film fabricated with additive 0 wt% (intrinsic $CsPbI_3$), 5 wt%, 12 wt%, and 21 wt%-CsBr/ $PbBr_2$ according to the concentrations of the additives CsBr and $PbBr_2$ in the $CsPbI_3$ precursor solution. In order to confirm the optoelectronic characteristics of the heterojunction film with perovskite/IGZO, a 20 nm IGZO film was deposited on a glass substrate by DC sputtering, and an 80 nm $CsPbI_xBr_{3-x}$ film was spincoated thereon to fabricate the all-inorganic heterojunction film. The spectra resulting from X-ray diffraction (XRD) and the X-ray photoemission spectroscopy (XPS) were

analyzed to confirm the change in crystallinity and chemical composition of the $CsPbI_xBr_{3-x}$ film according to the different concentrations of additives $CsBr/PbBr_2$ in the $CsPbI_3$ precursor solution (Fig. 3. 1). The XRD analysis in Fig. 3. 1a shows the phase transition tendency of the $CsPbI_xBr_{3-x}$ film fabricated with the different concentrations of additives $CsBr/PbBr_2$. The intrinsic $CsPbI_3$ (additive 0 wt%-$CsBr/PbBr_2$ in the $CsPbI_3$ precursor solution) film showed an orthorhombic structure referred to as the δ-phase [38]. The peak values of the XRD patterns located at 2θ = 22.821° and 26.521° were indexed to the (112) and (122) planes referred to as δ-phase. When the $CsPbI_xBr_{3-x}$ films were fabricated with the additives $CsBr/PbBr_2$ in the $CsPbI_3$ precursor solution, the $CsPbI_xBr_{3-x}$ films transformed into the cubic structure of the α-phase from the orthorhombic structure of the δ-phase. The XRD peaks of the $CsPbI_xBr_{3-x}$ film fabricated with the additive 5 wt%-$CsBr/PbBr_2$ at 14.321°, 20.31°, and 29.21° were assigned to the (100), (110) and (200) planes, respectively, which represented the α-phase. The $CsPbI_xBr_{3-x}$ film fabricated with the additive 12 wt%-$CsBr/PbBr_2$ increased the intensity of the peaks of the (100), (110) and (200) related to the a-phase, and the peaks of the δ-phase completely disappeared. The strength of peaks for the (100), (110) and (200) planes of the $CsPbI_xBr_{3-x}$ film fabricated with the additive 21 wt%-$CsBr/PbBr_2$ was somewhat lower than that of the $CsPbI_xBr_{3-x}$ film fabricated with the additive 12

wt%-CsBr/$PbBr_2$. Fig. 3. 1b shows the magnification figure of the XRD (200) peak for $CsPbI_xBr_{3-x}$ fabricated with different concentrations of additives CsBr/$PbBr_2$ in the $CsPbI_3$ precursor solution. In general, the (200) plane of the α-$CsPbI_3$ was reported as $2\theta = 28.821°$ [39]. However, the value of 2θ at the (200) plane of the α-$CsPbI_xBr_{3-x}$ was shifted slightly higher than that at the (200) plane of the α-$CsPbI_3$. When the additives CsBr/$PbBr_2$ are added in the $CsPbI_3$ phase some of the I ions are replaced with Br ions in the perovskite phase because the atomic radius of Br is smaller than that of I, resulting in lattice shrinkage of the α-$CsPbI_xBr_{3-x}$ film [17]. Therefore, as the concentration of the additives CsBr/$PbBr_2$ in the $CsPbI_3$ precursor solution increases, the XRD peaks associated with the α-phase migrate at a slightly higher angle. The (200) plane of $CsPbIBr_2$ and $CsPbI_2Br$ was reported to be located at $2\theta = 30.151°$ and 29.501°, respectively [37, 40]. The 2θ value of the (200) plane for the $CsPbI_xBr_{3-x}$ films fabricated with 5 wt%, 12 wt%, and 21 wt%-CsBr/$PbBr_2$ additives in the $CsPbI_3$ precursor solution were found to be 29.21°, 29.461°, and 29.591°, respectively, which is close to that of the (200) plane of the $CsPbI_2Br$ film. Specifically, it can be said that the plane for the $CsPbI_xBr_{3-x}$ films fabricated with the additive 12 wt%-CsBr/$PbBr_2$ is the closest to the plane of $CsPbI_2Br$. The $CsPbI_xBr_{3-x}$ film fabricated with the additive 12 wt%-CsBr/$PbBr_2$ exhibited the smallest full width at halfwidth (FWHM) at the (200) plane, which suggests the

minimum size of the crystal. Fig. 3. 1c and d show the XPS spectra of I 3d and Br 3d according to the concentration of the additives CsBr/ $PbBr_2$. I $3d_{3/2}$ and I $3d_{5/2}$ peaks of the intrinsic $CsPbI_3$ film were assigned to 629.2 eV and 614.4 eV, respectively. As the concentration of $CsBr/PbBr_2$ additives increased from 0 wt% to 12 wt%, core level peaks for I 3d were assigned to 629.6 eV and 614.8 eV, indicating an increment of 0.4 eV binding energy. Similarly, Br $3d_{3/2}$ and Br $3d_{5/2}$ peaks of the $CsPbI_xBr_{3-x}$ film fabricated with additive 5%-$CsBr/PbBr_2$ were located at 68.83 eV and 67.83 eV, respectively, and when the additive concentration was increased to 12 wt%-$CsBr/PbBr_2$, Br 3d peaks were respectively shifted to 69.03 eV and 68.03 eV, which increased the binding energy by 0.2 eV. The increment of the binding energy of I 3d and Br 3d means that the binding force between I and Br increases at the $CsPbI_xBr_{3-x}$ structure, because the ionized Br of the $CsBr/PbBr_2$ additives in the $CsPbI_3$ precursor solution is smaller than I, resulting in lattice contraction when Br ions are inserted into $CsPbI_3$. The migration to a high binding energy according to the high concentration of $CsBr/PbBr_2$ additives contributes to keeping the crystalline phase of the $CsPbI_xBr_{3-x}$ stable. Therefore, the perovskite film fabricated with the additives $CsBr/PbBr_2$ in the $CsPbI_3$ precursor solution has the remarkable benefit of obtaining a stable α-$CsPbI_xBr_{3-x}$ film. Table 3. 1 summarizes the atomic ratio of Cs/Pb, (I + Br)/Pb and I/Br, quantified by XPS

signals of Cs 3d, Pb 4f, I 3d and Br 3d for the $CsPbI_xBr_{3-x}$ perovskite film with different concentrations of additives $CsBr/PbBr_2$. The intrinsic $CsPbI_3$ (additive 0 wt%-CsBr/ $PbBr_2$ in the $CsPbI_3$ precursor solution) shows an I/Pb ratio of 2.29 due to the δ-phase, which differs from the stoichiometric value of 3. On the other hand, the Cs/Pb ratio and (I + Br)/Pb of the $CsPbI_xBr_{3-x}$ film fabricated with the additive 12 wt%-$CsBr/PbBr_2$ exhibit stoichiometrically stable values of 1.03 and 2.76, respectively. The stability of the $CsPbI_xBr_{3-x}$ film fabricated with the additive 21 wt%-$CsBr/PbBr_2$ decreases stoichiometrically because the (I + Br)/Pb ratio is 2.52, which is lower than that of the $CsPbI_xBr_{3-x}$ film fabricated with additive 12 wt%-$CsBr/PbBr_2$. Therefore, since the $CsPbI_xBr_{3-x}$ film fabricated with additive 12 wt%-$CsBr/PbBr_2$ is stoichiometrically the most stable, the $CsPbI_xBr_{3-x}$ film is expected to constantly maintain the cubic structure of the α-phase.

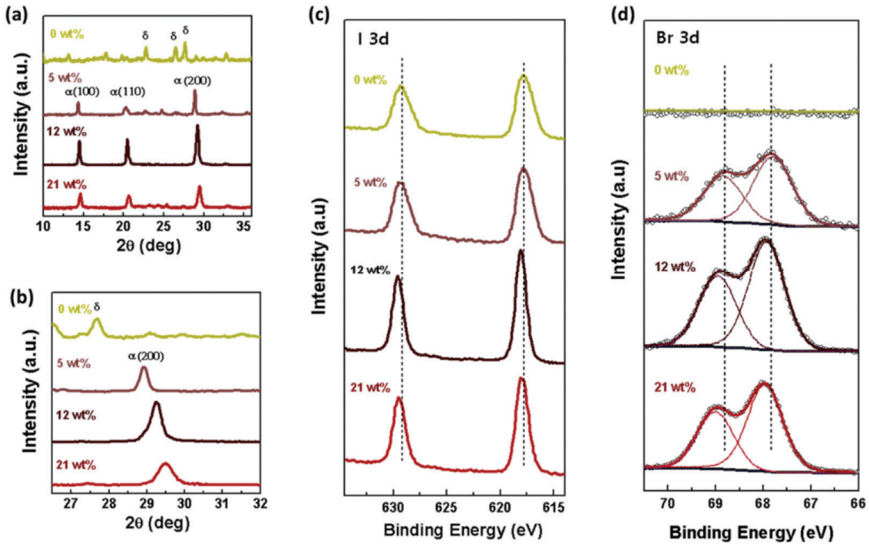

Figure 3. 2 (a) XRD patterns of $CsPbI_xBr_{3-x}$ perovskite films fabricated with different concentrations of additive $CsBr/PbBr_2$ (0 wt%, 5 wt%, 12 wt%, and 21 wt%) in the $CsPbI_3$ precursor solution. (b) Magnification of the (200) plane for the XRD patterns of $CsPbI_xBr_{3-x}$ perovskite films fabricated with different concentrations of additive $CsBr/PbBr_2$ (0 wt%, 5 wt%, 12 wt%, and 21 wt%) in the $CsPbI_3$ precursor solution. (c) I 3d and (d) Br 3d for XPS spectra of $CsPbI_xBr_{3-x}$ perovskite films fabricated with different concentrations of additive $CsBr/PbBr_2$ (0 wt%, 5 wt%, 12 wt%, and 21 wt%) in the $CsPbI_3$ precursor solution.

Concentration of additive $CsBr/PbBr_2$ (wt%)	Cs/Pb	(I + Br)/Pb	I/Br
0	0.94	2.29	—
5	1.03	2.47	0.13
12	1.03	2.76	0.30
21	0.97	2.52	0.45

Table 3. 1 Cs/Br, (I + Br)/Pb, and I/Br ratio of the $CsPbI_xBr_{3-x}$ perovskite films fabricated with different concentrations of additives $CsBr/PbBr_2$ in the $CsPbI_3$ precursor solution.

Photographs and filed-emission scanning electron microscopy (FE-SEM) images of heterojunction films with $CsPbI_xBr_{3-x}$/IGZO according to different concentrations of additives CsPb/$PbBr_2$ are shown in Fig. 3. 2a. The intrinsic $CsPbI_3$ (additive 0 wt%-CsBr/$PbBr_2$ in the $CsPbI_3$ precursor solution) film showed a yellow-colored δ-phase with an orthorhombic structure, and in the FE-SEM image, the film exhibited a large crystal structure. When the additives CsBr/$PbBr_2$ were added, the photographs show that the $CsPbI_xBr_{3-x}$ films were well-formed as the black a-phase. In addition, the FE-SEM images show the tendency for changing crystal size according to the concentration of additives CsBr/$PbBr_2$. For the $CsPbI_xBr_{3-x}$ film fabricated with the additive 12 wt%-CsBr/$PbBr_2$, the smallest crystal size and its dense structure were confirmed. Fig. 3. 2b and c show the UV-vis absorption spectra and optical bandgap derived from the Tauc plot for heterojunction films with $CsPbI_xBr_{3-x}$/IGZO according to the concentration of additives CsBr/$PbBr_2$ in the $CsPbI_3$ precursor solution, respectively. The intrinsic $CsPbI_3$ film exhibits an orthorhombic structure with δ-phase, which has absorption in the UV and blue regions (~430 nm) but does not absorb over the wide range of visible light, which corresponds to a bandgap of 2.8 eV. On the other hand, the $CsPbI_xBr_{3-x}$ film fabricated with the additive 5 wt%-CsBr/$PbBr_2$ absorbs up to the wavelength edge of 680 nm and has a peak at 400 nm which is associated with δ-

phase disappearance, indicating an α-phase with the bandgap of 1.77 eV. Also, when the concentration of the additives CsBr/ $PbBr_2$ is increased from 12 wt% to 21 wt%, the end of the absorption band shifts somewhat towards the blue wavelength region from 700 nm to 670 nm, which is related to the change in bandgap (from 1.82 eV to 1.88 eV). These $CsPbI_xBr_{3-x}$ perovskite films fabricated with additives $CsBr/PbBr_2$ are still sufficient to be used as absorption layers which absorb the wide range of visible light.

The $CsPbI_xBr_{3-x}$ film with the additives $CsBr/PbBr_2$ was found to form an α-phase film by the low-temperature process and we evaluated the high stability of the perovskite films without any phase transition under ambient conditions (20 °C, 25% RH) (Fig. 3. 3). Fig. 3. 3a shows the photographs of the $CsPbI_xBr_{3-x}$ films fabricated with different concentrations of additives $CsBr/PbBr_2$ over 1 month under ambient conditions (20 °C, 25% RH). The $CsPbI_xBr_{3-x}$ film fabricated with 5 wt%-$CsBr/PbBr_2$ transformed from black to yellow after 3 days, resulting in phase transition and deterioration. On the other hand, the $CsPbI_xBr_{3-x}$ film fabricated with the additive 12 wt%-$CsBr/PbBr_2$ stably retained its black color over 1 month, and the color of the $CsPbI_xBr_{3-x}$ film fabricated with the additive 21 wt%-$CsBr/PbBr_2$ was slightly deteriorated as compared with the color of the $CsPbI_xBr_{3-x}$ film fabricated with the additive 12 wt%-$CsBr/PbBr_2$. As shown in Fig. 3. 3b, the

$CsPbI_xBr_{3-x}$ film fabricated with the additive 12 wt%-$CsBr/PbBr_2$ was found to be the most stable by comparing its absorbance spectra when it was just formed to the spectra produced after 1 month under ambient conditions (20 °C, 25% RH). In addition, from the XRD analysis, the $CsPbI_xBr_{3-x}$ film fabricated with the additive 12 wt%-$CsBr/PbBr_2$ shows excellent stability because there is no transition of crystallinity between the as-formed film and the film after 1 month. As mentioned in the XRD and XPS results in Fig. 3. 1, the $CsPbI_xBr_{3-x}$ film fabricated with the additive 12 wt%-$CsBr/PbBr_2$ has the highly stable crystallinity because of the increasing binding energy of I and Br by adding Br ions. Also, since the (I + Br)/Pb ratio of the film is close to 3, it is stoichiometrically stable. From these results, I confirm that the $CsPbI_2Br$ film fabricated with the additive 12 wt%-$CsBr/PbBr_2$ had very high stability without any phase transition over 1 month under ambient conditions (20 °C, 25% RH).

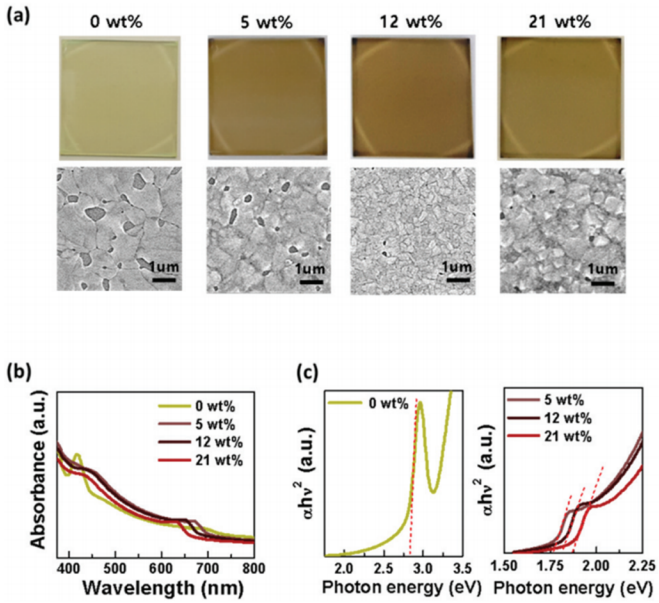

Figure 3. 2 (a) Photographs, FE-SEM Images, (b) UV-vis absorption, and (c) bandgap of the $CsPbI_xBr_{3-x}$ perovskite films fabricated with different concentrations of additive $CsBr/PbBr_2$ (0 wt%, 5 wt%, 12 wt%, and 21 wt%) in the $CsPbI_3$ precursor solution.

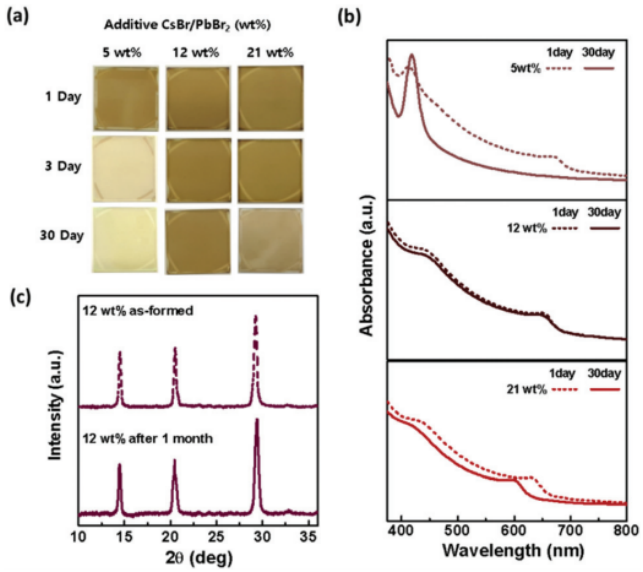

Figure 3. 3 (a) Photographs and (b) UV-vis absorption of $CsPbI_xBr_{3-x}$ perovskite films fabricated with different concentrations of additive $CsBr/PbBr_2$ (5 wt%, 12 wt%, 21 wt%) in the $CsPbI_3$ precursor solution for 1 month, showing phase transition under ambient conditions (20 °C, 25% RH). (c) XRD patterns of the $CsPbI_xBr_{3-x}$ film fabricated with additive 12 wt%-$CsBr/PbBr_2$ in the $CsPbI_3$ precursor solution, measured when just formed and after 1 month.

3.3 Optoelectrical properties and stabilities according to the 12 wt%-$CsBr/PbBr_2$ in the $CsPbI_3$ precursor solution

Using the $CsPbI_2Br$ film fabricated with the additive 12 wt%- $CsBr/PbBr_2$ in the $CsPbI_3$ precursor solution, which has high stability without any phase transition under ambient conditions (20 °C, 25% RH) and absorbs the entire visible light region, I fabricated a visible light detector based on a heterojunction phototransistor with $CsPbI_2Br$/IGZO, which acted as the absorption layer and charge transfer layer, respectively (Fig. 3. 4). Heavily p-doped silicon wafers, SiO_2, and IGZO were used as gate electrodes, gate insulators, and electron transfer layers, respectively. A $CsPbI_2Br$ film of 80 nm thickness with a visible light absorption layer was formed on IGZO using low-temperature solution processing (90 °C) (Fig. 3. 5). Finally, the source and drain metal of the phototransistor were patterned with Ti–Al–Ti (20 nm–100 nm–20 nm) and its width and channel were defined as 1000 mm and 50 mm, respectively. Also, in order to confirm the characteristics of conventional IGZO and single-layered $CsPbI_2Br$ perovskite phototransistors, reference devices were additionally analyzed (Fig. 3. 4b and c). The gate voltage of the phototransistor was swept from 50 V to 50 V and the transfer characteristics were measured.

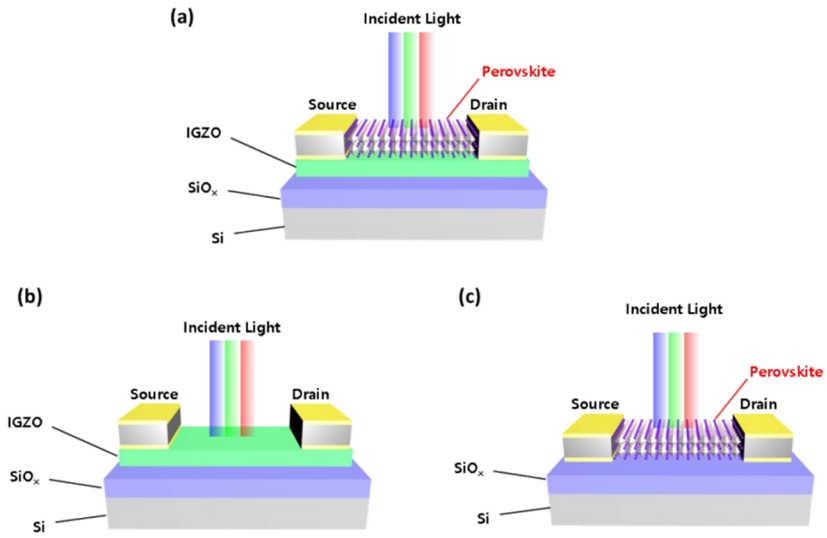

Figure 3. 4 The schematic of the device structures. (a) double-layered heterojunction phototransistor with perovskite/IGZO. (b) conventional IGZO phototransistor. (c) single-layered $CsPbI_2Br$ perovskite phototransistor.

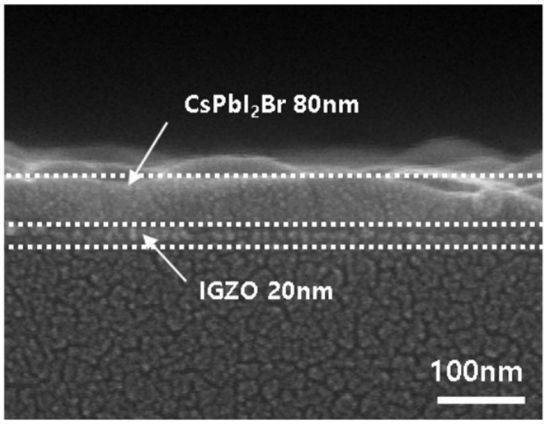

Figure 3. 5 FESEM cross section image of the heterojunction film with $CsPbI_2Br$ and IGZO.

The transistor characteristics of the conventional IGZO phototransistor and the heterojunction phototransistor with $CsPbI_2Br$ (additive 12 wt%-$CsBr/PbBr_2$ in the $CsPbI_3$ precursor solution)/IGZO at the dark state are shown in Table 3. 2. The two devices showed similar characteristics in most of the parameters in the dark state. However, the I_{on} and linear mobility of the heterojunction phototransistors are slightly lower than those of conventional IGZO. Because the perovskite layer capped on the IGZO is considered to be a resistor in the absence of light, the total sheet resistance of $CsPbI_2Br$/IGZO increases slightly in the channel region. Even so, these parameters may not mean a serious deterioration of the phototransistor. Under light illumination conditions, the devices were evaluated by irradiating 1 mW /cm^2 light of 635 nm, 532 nm, and 450 nm of red, green, and blue with a LED light. As shown in Fig. 3. 6a, the off current of the conventional IGZO phototransistor at the only 450 nm wavelength under visible light irradiation was slightly higher than that of the dark state. Although the IGZO has the wide bandgap of 3.5 eV, the IGZO phototransistor is explained by the phenomenon that the localized oxygen vacancy near the valence band of IGZO is ionized by the blue light (450 nm) and photo-generated electrons are transferred within the IGZO [41]. On the other hand, as shown in Fig. 3.6b, at the visible light irradiation, the single-layered $CsPbI_2Br$ perovskite phototransistor showed no difference in drain current compared to the

dark state regardless of gate voltage sweep. This means that the excitons generated by the light irradiation cannot move to the lateral direction in the single-layered $CsPbI_2Br$ perovskite film from the source to the drain, and the recombination time of the excitons is shorter than the time for moving the channel between the source and drain so that the single-layered $CsPbI_2Br$ perovskite film has a limited role as a channel layer. The double-layered heterojunction phototransistor with intrinsic $CsPbI_3$ (additive 0 wt%-$CsBr/PbBr_2$ in the $CsPbI_3$ precursor solution)/IGZO exhibited remarkably low off-current at the negative gate voltage in the dark state and showed a higher drain current (I_{ds}) than the conventional IGZO phototransistor at the blue light irradiation. In the case of red and green light irradiation, the heterojunction phototransistor with intrinsic $CsPbI_3$/IGZO did not generate any photocurrent like the conventional IGZO phototransistor (Fig. 3. 6c). It is because the intrinsic $CsPbI_3$ rapidly transitions to the δ-phase after fabrication and is absorbed only at the wavelength regions below 430 nm as mentioned in Fig. 3. 2. On the other hand, as shown in Fig. 3. 6d, the double-layered heterojunction phototransistor with $CsPbI_2Br$/IGZO shows a higher current level of 10^5 than I_{ds} in the dark state upon all regions of visible light at the negative gate voltage. The transfer characteristics of the doublelayered heterojunction phototransistor according to concentrations of additives $CsBr/PbBr_2$ in the $CsPbI_3$ precursor

solution upon visible light irradiation are shown in Fig. 3. 7. Because the $CsPbI_2Br$ perovskite film absorbs at the wide range of visible light, the heterojunction phototransistor with $CsPbI_2Br$/IGZO showed high current level characteristics in all red, green and blue lights. Fig. 3. 6e and f show energy band diagrams and current path according to the gate voltage bias of the heterojunction phototransistor with $CsPbI_2Br$/IGZO. We suggest the current flow mechanism for different V_g ($V_g < V_{th}$, $V_g > V_{th}$) in the energy band diagram of the heterojunction phototransistor with $CsPbI_2Br$/IGZO. The bandgap and work function are fitted by measuring the absorption peaks (Fig. 3. 8a and b) and UPS (Fig. 3. 8c and d) of $CsPbI_2Br$ and IGZO, and the flat energy band diagram of the heterojunction phototransistor is plotted in Fig. 3. 8e . When the gate voltage is in the off state with a negative bias ($V_g < V_{th}$), electrons excited by light in the $CsPbI_2Br$ layer of the heterojunction will not pass through the IGZO/SiO_2 interface. It is expected that electrons will only move along the lateral direction in the back channel of the IGZO layer located at the $CsPbI_2Br$/IGZO interface between the source and drain. Under the dark state, when the gate voltage is in the on-state with a positive bias ($V_g > V_{th}$), the accumulation state occurs in the IGZO layer of the heterojunction and electrons are transferred along the front channel of the IGZO layer located in the IGZO/SiO_2 interface.

Structures	Linear Mob. ($cm^2V^{-1}s^{-1}$)	S.S ($Vdec^{-1}$)	I_{off} (A)	I_{on} (A)
Conventional IGZO	15.11 ± 0.59	0.27 ± 0.04	(1.05 ± 0.05) × 10^{-12}	(2.40 ± 0.2) × 10^{-5}
$CsPbI_2Br$ / IGZO	12.71 ± 0.46	0.36 ± 0.07	(1.03 ± 0.04) × 10^{-12}	(1.29 ± 0.4) × 10^{-5}

Table 3. 2 Device characteristics of conventional IGZO phototransistor and heterojunction phototransistor with $CsPbI_2Br$ / IGZO at the dark state.

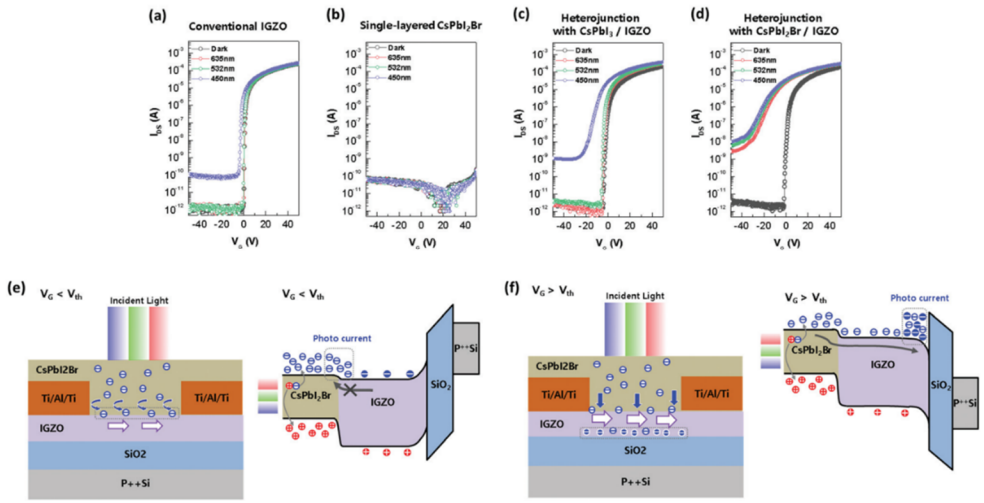

Figure 3. 6 Transfer characteristics of (a) conventional IGZO phototransistor, (b) single-layered $CsPbI_2Br$ (additive 12 wt%-$CsBr/PbBr_2$ in the $CsPbI_3$ precursor solution) perovskite phototransistor, (c) heterojunction phototransistor with intrinsic $CsPbI_3$ (additive 0 wt%-$CsBr/PbBr_2$ in the $CsPbI_3$ precursor solution)/IGZO, and (d) heterojunction phototransistor with $CsPbI_2Br$ (additive 12 wt%-$CsBr/PbBr_2$ in the $CsPbI_3$ precursor solution)/IGZO at various wavelengths of light illumination (dark, 450 nm, 532 nm and 635 nm) at V_{DS} = 1 V. Schematic diagrams of the current flows based on an energy band diagram in heterojunction with $CsPbI_2Br$/IGZO phototransistor channel at (e) $V_g < V_{th}$ and (f) $V_g > V_{th}$ under the visible light illumination.

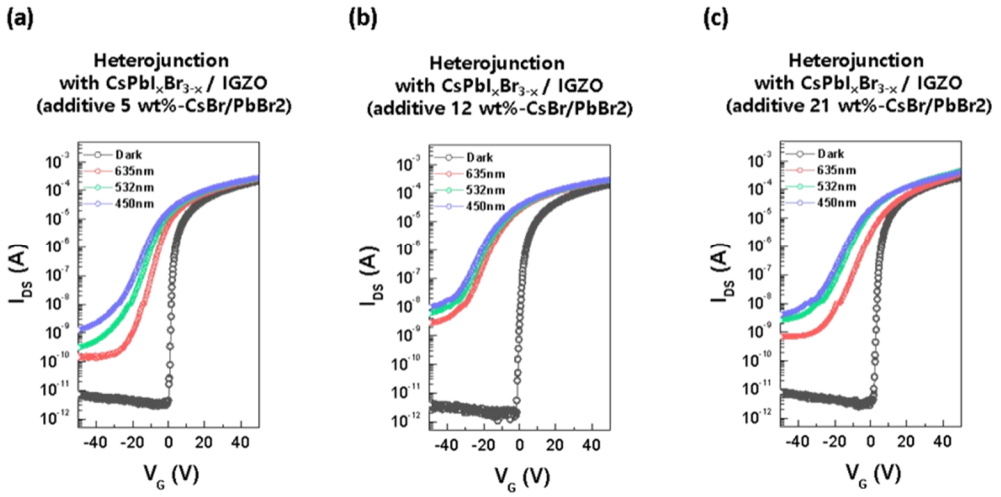

Figure 3. 7 Transfer characteristics of heterojunction phototransistors with $CsPbI_xBr_{3-x}$ / IGZO under dark and light irradiation (450 nm, 532 nm, and 635 nm wavelength of 1 mW/cm^2 power density) at V_{DS} = 1 V, which perovskite films were fabricated with the different concentration of additives (a) 5 wt%-, (b) 12 wt%-, and (c) 21 wt%-CsBr/$PbBr_2$ in the $CsPbI_3$ precursor solution.

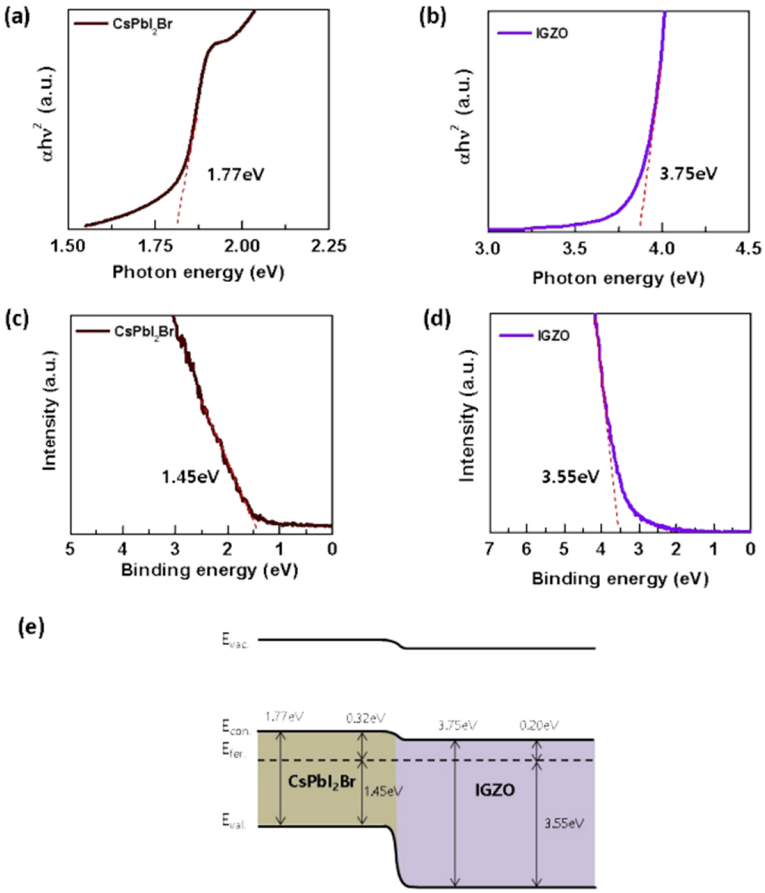

Figure 3. 8 Bandgap of the (a) $CsPbI_2Br$ and (b) IGZO by absorption peak. Work function of (c) $CsPbI_2Br$ and (d) IGZO by UPS. (e) Energy band diagram of heterojunction with $CsPbI_2Br$ / IGZO.

Upon light illumination, photo-generated electrons from the $CsPbI_2Br$ layer move along the back channel of the IGZO layer, resulting in a higher electron concentration, which will increase the I_{ds}. The main photo-parameters of the phototransistor is the responsivity (R) and the specific detectivity (D*), which are calculated according to the following equations (eq. 3. 3. 1 and 3. 3. 2).

$$R = \frac{J_{ph}}{P_{in}} = \frac{(I_{photo} - I_{dark})/A_{TFT}}{P_{in}/A_{LED}}, \quad (3.\,3.\,1)$$

$$D^* = \frac{R}{(2qJ_{dark})^{1/2}} = \frac{R}{(2qI_{dark}/A_{TFT})^{1/2}}, \quad (3.\,3.\,2)$$

where J_{ph} is the photocurrent density, P_{in} is the power density of incident light, I_{photo} and I_{dark} are photocurrents under light illumination and dark state, A_{TFT} and ALED are the effective areas of the phototransistor and the LED light source, and q is the elementary charge. Fig. 3. 9 shows the responsivity and detectivity at a drain voltage of 1 V upon a red light power density of 1 mW/cm^2 . As mentioned in the FE-SEM, XRD, and XPS analyses, the $CsPbI_2Br$ perovskite film fabricated with additive 12 wt%-$CsBr/PbBr_2$ is the most stoichiometrically stable and exhibits high crystallinity due to the increased binding force between I and Br. The heterojunction phototransistor with $CsPbI_2Br$ (additive 12 wt%-$CsBr/PbBr_2$ in the $CsPbI_3$

precursor solution)/IGZO is confirmed to yield excellent photo-parameter characteristics. Fig. 3. 10a shows the responsivity and detectivity of the heterojunction phototransistor including the $CsPbI_xBr_{3-x}$ film fabricated with different concentrations of additives $CsBr/PbBr_2$ in the $CsPbI_3$ precursor solution at $V_g = 5$ V upon visible light irradiation of wavelengths between 450 nm and 635 nm with the light power density of 1 mW/cm^2 . The heterojunction phototransistor with intrinsic $CsPbI_3$ (additive 0 wt%-$CsBr/PbBr_2$ in the $CsPbI_3$ precursor solution)/IGZO exhibits negligible responsivity and detectivity at 532 nm and 635 nm wavelengths because the intrinsic $CsPbI_3$ film with d-phase absorbs under the wavelength of 430 nm. On the other hand, the $CsPbI_2Br$ perovskite film absorbs the wavelengths of entire visible light regions, so the heterojunction phototransistor with $CsPbI_2Br$/IGZO exhibits high responsivity and detectivity characteristics at the wide range of visible light. The heterojunction phototransistor including $CsPbI_2Br$/IGZO was found to have a responsivity of 26.48 A/W , a detectivity of 8.42×10^{14} Jones, sensitivity of 8.71×10^6 , and external quantum efficiency (EQE) of 51% (Table 3. 2). Fig. 3. 10b shows the transfer curve according to the light power density of red light for a heterojunction phototransistor with $CsPbI_2Br$/IGZO. The heterojunction phototransistor with $CsPbI_2Br$/IGZO is confirmed to have a high level of photocurrent according to the increase of light power density. Conventional

IGZO phototransistors exhibit a slow response characteristic of rising and falling time for several seconds after the light is turned on and off, which is known as persistence photocurrent (PPC) phenomenon and is caused by ionization of the oxygen vacancy in the IGZO layer only under blue light irradiation [7, 42]. Fig. 3. 10c shows that the heterojunction phototransistors with $CsPbI_2Br$/IGZO are relatively free from the limitation of the PPC phenomenon. 450 nm, 532 nm, and 635 nm light with a power density of 0.04 mW/cm^2 at a fixed V_g = 5 V and V_{DS} = 1 V are periodically irradiated at 10 s intervals in a heterojunction phototransistor with $CsPbI_2Br$/IGZO. The heterojunction phototransistor exhibits a constant and stable transient response during longterm measurements of periodic on–off light irradiation. Rising time and falling time are defined as the interval time between 10% and 90% of the peak value of the photocurrent when the light is turned on and off. The heterojunction phototransistor shows a fast transient response with rising time (0.61 s) and falling time (0.79 s) under red light (635 nm). Even so, the heterojunction phototransistor guarantees better response time than that of the conventional IGZO phototransistor under the blue light region (450 nm) in Fig. 3. 11. We assume that the time of transient response with the heterojunction is strongly reduced by the photo-generated electrons, immediately filling local oxygen vacancies near the ionized valence band caused by the PPC phenomenon of the

IGZO layer under blue light. As shown in Fig. 3. 10e, we evaluated the stability of the $CsPbI_2Br$/IGZO heterojunction phototransistor and intrinsic $CsPbI_3$/IGZO heterojunction phototransistor in the air. The photocurrent of the heterojunction phototransistors was measured over 1 month under light irradiation with a wavelength of 635 nm under ambient conditions (20 1C, 25% RH). The photocurrent of the heterojunction phototransistor with intrinsic $CsPbI_3$/IGZO deteriorated within 3 days because δ-phase $CsPbI_3$ absorbed moisture and was easily degraded, whereas the heterojunction phototransistor with $CsPbI_2Br$/IGZO showed a stable photocurrent over 1 month, which is the same as the result of stability for the $CsPbI_2Br$ film fabricated with additive 12 wt%-$CsBr/PbBr_2$ in Fig. 3. 3. As mentioned with the XRD and XPS analyses in Fig. 3. 1, because the addition of $CsBr/PbBr_2$ in the $CsPbI_3$ increases the binding energy between I and Br in the $CsPbI_2Br$ structure, the $CsPbI_2Br$ absorption layer keeps the α-phase stable for a long time without a phase transition.

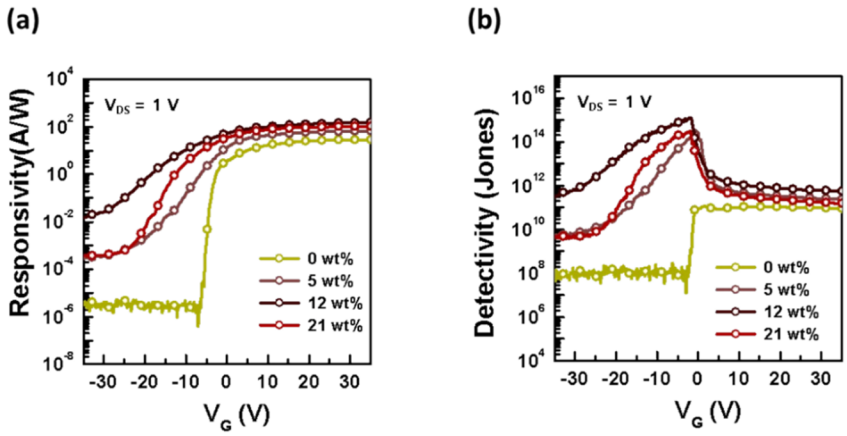

Figure 3. 9 (a) Responsivity and (b) Detectivity of heterojunction phototransistor with CsPbI2Br (additive 12 wt%-PbBr/$CsBr_2$ in the $CsPbI_3$ precursor solution) / IGZO under the 635 nm light illumination (power density = 1 mW/cm^2) at VDS = 1 V.

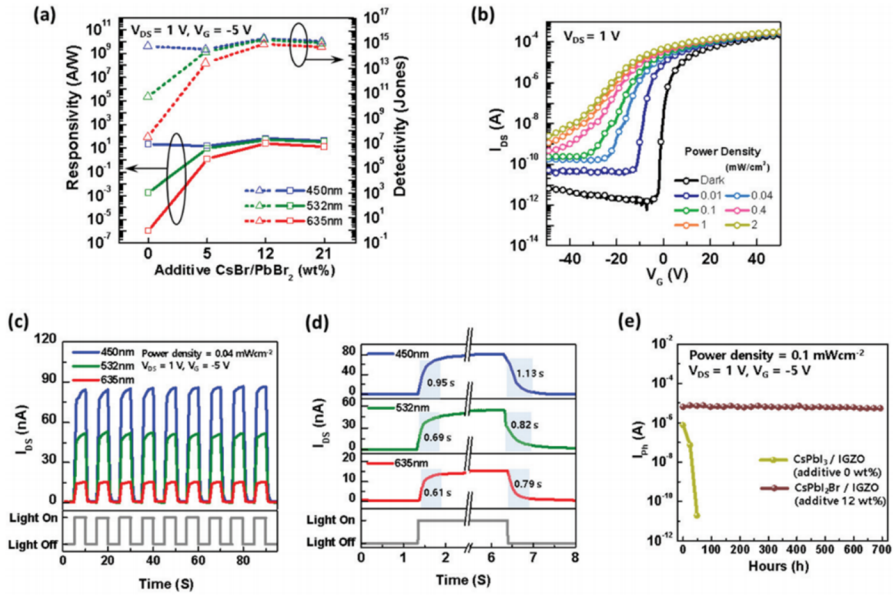

Figure 3. 10 (a) Responsivity and detectivity of the heterojunction phototransistor with $CsPbI_2Br$ (additive 12 wt%-$PbBr/CsBr_2$ in the $CsPbI_3$ precursor solution)/IGZO at various wavelengths of light illumination (dark, 450 nm, 532 nm and 635 nm) at V_{DS} = 1 V. (b) Transfer characteristics of the heterojunction phototransistor with $CsPbI_2Br$/IGZO under different incident light intensities at 635 nm (V_{DS} = 1 V). (c) Transient response of the heterojunction phototransistor with $CsPbI_2Br$/IGZO under 450 nm, 532 nm and 635 nm pulse light at a constant V_g = 5 V, V_{ds} = 1 V. (d) Enlarged 1 cycle figure of the transient response of the heterojunction phototransistor under 450 nm, 532 nm and 635 nm pulse light. (e) I_{ds} measurements of the heterojunction phototransistor with $CsPbI_2Br$/IGZO and the heterojunction phototransistor with intrinsic $CsPbI_3$/IGZO for 1 month under ambient conditions (20 °C, 25% RH).

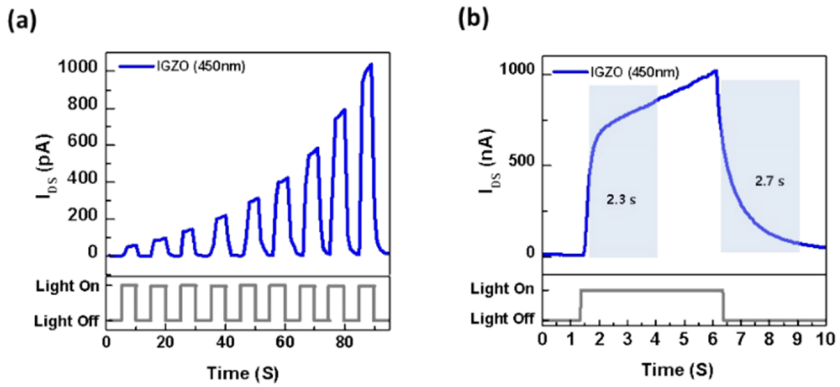

Figure 3. 11 (a) Transient response of conventional IGZO phototransistor under 450 nm pulse light at a constant V_g =-5 V, V_{ds} = 1 V. (b) Enlarged 1 cycle figure of the transient response of conventional IGZO phototransistor under 450 nm pulse light.

3.4 Conclusion

In this chapter, I developed an all-inorganic perovskite $CsPbI_xBr_{3-x}$ film with good optical sensing performance, manufactured using a low-temperature process at 90 °C, and even ensured its excellent long term stability over 1 month under ambient conditions (20 °C, 25% RH). Furthermore, using the heterojunction film with the highly stable perovskite $CsPbI_xBr_{3-x}$/IGZO, we fabricated a heterojunction phototransistor detecting the wide range of visible light. We investigated the crystallinity and phase retention behaviors of the perovskite $CsPbI_xBr_{3-x}$ film according to the concentration of the additives $CsBr/PbBr_2$ in the $CsPbI_3$ precursor solution with a low-temperature process. Through the electrical and chemical analyses, we found the most stoichiometrically stable $CsPbI_xBr_{3-x}$ film, which was fabricated with 12 wt% additives $CsBr/PbBr_2$ in the $CsPbI_3$ precursor solution. It was confirmed that the stability was maintained by increasing the binding energy while replacing I ions with Br ions, which have a smaller atomic radius, at room temperature. The heterojunction phototransistor with $CsPbI_2Br$/IGZO exhibited a responsivity of 26 A/W , a detectivity of 8.42×10^{14} Jones and an external quantum efficiency (EQE) of 51% at the red light power density of 1 mW/cm^2 , which expanded the detecting range from the ultraviolet to the visible light region. At light

irradiation into the heterojunction phototransistor, the excitons photo-generated from $CsPbI_2Br$ were transported along the IGZO back channel, which guaranteed a shorter response time (0.79 s) than that of the conventional IGZO phototransistor. In addition, the heterojunction phototransistor with $CsPbI_2Br$/IGZO showed excellent stability over 1 month under ambient conditions (20 °C, 25% RH). This research provides a promising way to enhance the stability of all-inorganic perovskite $CsPbI_xBr_{3-x}$ films and provides strong inspiration for the application of perovskite heterojunction phototransistors.

3.5 Experimental details

Precursor solution synthesis. To synthesize the perovskite $CsPbI_xBr_{3-x}$ precursor solution, I purchased powdered CsI (99.999%), PbI_2 (99%), CsBr (99.999%), $PbBr_2$ (99.999%) and DMSO (99.5%) solvent from Sigma Aldrich. In order to synthesize perovskite $CsPbI_xBr_{3-x}$ precursors with different I and Br ratios, at first, 0.4 M precursor solution was prepared by completely dissolving CsI and PbI_2 powder (a molar ratio of 1 : 1) in DMSO. And then, the additive of CsBr and $PbBr_2$ (1 : 1 molar ratio) with different weight ratios (0 wt%, 5 wt%, 12 wt% and 21 wt% with relating to 0.4 M) was added into the $CsPbI_3$ precursor solution, respectively, which was stirred at 500 rpm for 24 h.

Fabrication of the phototransistor devices. To fabricate the inverted-stacker type phototransistor, the heavily doped p-type Si wafer (P^{++}-Si) with a thermally grown 200 nm SiO_2 layer was sequentially immersed in detergent, deionized water, acetone, and isopropyl alcohol, and ultrasonically cleaned for 10 min. The IGZO film with a thickness of 20 nm was deposited on a SiO_2/Si substrate via sputtering with radiofrequency (RF) power using an IGZO target consisting of In_2O_3, ZnO, and Ga_2O_3 at a molar ratio of 1 : 1 : 1, respectively. At this time, the RF sputtering power of the target was fixed at 90 W under 10^6 Torr at room temperature. The

sputtered IGZO films were annealed in air for 425 °C and for 90 s using a rapid thermal annealing method. The Ti–Al–Ti source and drain electrodes were deposited at 20 nm–100 nm–20 nm thickness using a vacuum thermal evaporation system at 10^6 Torr pressure. To make the substrate surface hydrophilic, the substrate was irradiated with UV–O_3 for 10 min. The $CsPbI_xBr_{3-x}$ precursor solutions were spin-coated on the substrate at 3500 rpm for 45 s in an N_2-filled glove box. Then, after waiting for 3 min, the spin-coated film was baked at 90 °C for 5 min on a hot-plate to obtain a perovskite film. The width and length of the phototransistor were 1000 mm and 50 mm, and all phototransistors were patterned using photolithography and a wet etching process to prevent current leakage.

Measurement and analysis. The absorption and bandgap of the IGZO and $CsPbI_xBr_{3-x}$ films were measured from 300 to 800 nm using ultravioletvisible (UV-vis) spectroscopy (Lambda 35, PerkinElmer). The crystallinity and morphology of the $CsPbI_xBr_{3-x}$ films were obtained using field-emission scanning electron microscopy (FE-SEM, S-4800, Hitachi) and X-ray diffraction (XRD, D8 Advance, Bruker Co.) executed with Cu-Ka radiation (l = 1.54 Å) at 40 kV and 150 mA (6 kW) with a grazing-incidence mode. X-ray photoelectron spectroscopy (XPS) and ultraviolet photoelectron spectroscopy (UPS) were used to analyze the chemical

properties of $CsPbI_xBr_{3-x}$ and IGZO films (AXIS SUPRA, Kratos). The transfer characteristics of heterojunction phototransistors were measured with a semiconductor parameter analyzer (4155B, KEYSIGHT) in the dark and at visible light irradiation using LED light sources (STF0A36C, SSC).

3.6Reference

[1] Socratous, J. et al. Electronic structure of low-temperature solution-processed amorphous metal oxide semiconductors for thin-film transistor applications. *Adv. Funct. Mater.* **25**, 1873-1885 (2015)

[2] Jo, J. -W. et al. Highly stable and imperceptible electronics utilizing photoactivated heterogeneous sol-gel metal–oxide dielectrics and semiconductors. *Adv. Mater.* **27**, 1182-1188 (2015)

[3] Yu, X. et al. Metal oxides for optoelectronic applications. *Nat. Mater.* **15**, 383-396 (2016)

[4] Fortunato, E. et al. Oxide semiconductor thin-film transistors: A review of recent advances. *Adv. Mater.* **24**, 2945-2986 (2012)

[5] Nomura, K. et al. Room-temperature fabrication of transparent flexible thin-film transistors using amorphous oxide semiconductors. *Nature* **432**, 488 (2004)

[6] Kim, Y. -H. et al. Flexible metal-oxide devices made by room-temperature photochemical activation of sol–gel films. *Nature* **489**, 128-132 (2012)

[7] Jeon, S. et al. Gated three-terminal device architecture to eliminate persistent photoconductivity in oxide semiconductor photosensor arrays. *Nat. Mater.* **11**, 301-305 (2012)

[8] Ahn, C. H. et al. High photosensitivity and wide operation voltage in two-dimensional CdS nano-crystal layer embedded a-InGaZnO hybrid phototransistors. *J. Alloys Compd.* **725**, 891-898 (2017)

[9] Hwang, D. K. et al. Ultrasensitive PbS quantum-dot-sensitized InGaZnO hybrid photoinverter for near-infrared detection and imaging with high photogain. *NPG Asia Mater.* **8**, e233 (2016)

[10] Liu, X. et al. Photo-modulated thin film transistor based on dynamic charge transfer within quantum-dots-InGaZnO interface. *Appl. Phys. Lett.* **104**, 113501 (2014)

[11] Zhai, Y. et al. Investigation of photocurrent transient variation in Au nanoparticles-decorated IGZO phototransistor. *Phys. E* **113**, 92-96 (2019)

[12] Park, S. W. et al. Enhancement of near-infrared detectability from InGaZnO thin film transistor with MoS_2 light absorbing layer. *Nanotechnology* **28**, 475206 (2017)

[13] Yang, J. et al. MoS_2–InGaZnO Heterojunction Phototransistors with Broad Spectral Responsivity. *ACS Appl. Mater. Interfaces* **8**, 8576-8582 (2016)

[14] Pei, Z. High-responsivity and high-sensitivity graphene dots/a-IGZO thin-film phototransistor. *IEEE Electron Device Lett.* **36**, 44-46 (2015)

[15] Zhu, H. et al. One-step synthesis of graphene quantum dots from defective CVD graphene and their application in IGZO UV thin film phototransistor. *Carbon N. Y.* **100**, 201-207 (2016)

[16] Yi, C. et al. Entropic stabilization of mixed A-cation ABX_3 metal halide perovskites for high performance perovskite solar cells. *Energy Environ. Sci.* **9**, 656-662 (2016)

[17] Miyata, A. et al. Direct measurement of the exciton binding energy and effective masses for charge carriers in organic–inorganic tri-halide perovskites. *Nat. Phys.* **11**, 582-588 (2015)

[18] Umari, P. et al. Infrared dielectric screening determines the low exciton binding energy of metal-halide perovskites. *J. Phys. Chem. Lett.* **9**, 620-627 (2018)

[19] Chen, Y. et al. Large-area perovskite solar cells – a review of recent progress and issues. *RSC Adv.* **8**, 10489-10508 (2018)

[20] Sutton, R. J. et al. Bandgap-tunable cesium lead halide perovskites with high thermal stability for efficient solar cells. *Adv. Energy Mater.* **6**, 1502458 (2016)

[21] Dou, L. et al. Solution-processed hybrid perovskite photodetectors with high detectivity. *Nat. Commun.* **5**, 5404 (2014)

[22] Liu, C. et al. PbS quantum dots-induced trap-assisted charge injection in

perovskite photodetectors. *Nano Energy* **30**, 27-35 (2016)

[23] Chen, S. et al. A flexible UV–Vis–NIR photodetector based on a perovskite/conjugated-polymer composite. *Adv. Mater.* **28**, 5969-5974 (2016)

[24] Dong, Y. et al. Improving all-inorganic perovskite photodetectors by preferred orientation and plasmonic effect. *Small* **12**, 5622-5632 (2016)

[25] Qian, L. et al. A solution-processed high-performance phototransistor based on a perovskite composite with chemically modified graphenes. *Adv. Mater.* **29**, 1606175 (2017)

[26] Yu, Y. et al. Broadband phototransistor based on $CH_3NH_3PbI_3$ perovskite and PbSe quantum dot heterojunction. *J. Phys. Chem. Lett.* **8**, 445-451 (2017)

[27] Tak, Y. J. et al. Boosting visible light absorption of metal-oxide-based phototransistors via heterogeneous In–Ga–Zn–O and $CH_3NH_3PbI_3$ films. *ACS Appl. Mater. Interfaces* **10**, 12854-12861 (2018)

[28] Xu, X. et al. Enhanced detectivity and suppressed dark current of perovskite–InGaZnO phototransistor via a PCBM interlayer. *ACS Appl. Mater. Interfaces* **10**, 44144-44151 (2018)

[29] Conings, B. et al. Intrinsic thermal instability of methylammonium lead trihalide perovskite. *Adv. Energy Mater.* **5**, 1500477 (2015)

[30] Stoumpos, C. C. et al. Semiconducting tin and lead iodide perovskites with organic cations: phase transitions, hgh mobilities, and near-infrared photoluminescent properties. *Inorg. Chem.* **52**, 9019-9038 (2013)

[31] Christians, J. A. et al. Transformation of the excited state and photovoltaic efficiency of $CH_3NH_3PbI_3$ perovskite upon controlled exposure to humidified air. *J. Am. Chem. Soc.* **137**, 1530-1538 (2015)

[32] Li, B. et al. Surface passivation engineering strategy to fully-inorganic cubic $CsPbI_3$ perovskites for high-performance solar cells. *Nat. Commun.* **9**, 1076 (2018)

[33] Xiang, S. et al. Highly air-stable carbon-based α-$CsPbI_3$ perovskite solar cells with a broadened optical spectrum. *ACS Energy Lett.* **3**, 1824-1831 (2018)

[34] Dastidar, S. et al. Quantitative phase-change thermodynamics and metastability of perovskite-phase cesium lead iodide. *J. Phys. Chem. Lett.* **8**, 1278-1282 (2017)

[35] Swarnkar, A. et al. Quantum dot–induced phase stabilization of α-$CsPbI_3$ perovskite for high-efficiency photovoltaics. *Science* **354**, 92-95 (2016)

[36] Hoffman, J. B. et al. Transformation of sintered $CsPbBr_3$ nanocrystals to cubic $CsPbI_3$ and gradient $CsPbBr_xI_{3-x}$ through halide exchange. *J. Am. Chem. Soc.* **138**, 8603-8611 (2016)

[37] Nam, J. K. et al. Unveiling the crystal formation of cesium lead mixed-halide perovskites for efficient and stable solar cells. *J. Phys. Chem. Lett.* **8**, 2936-2940 (2017)

[38] Luo, P. et al. Solvent engineering for ambient-air-processed, phase-stable $CsPbI_3$ in perovskite solar cells. *J. Phys. Chem. Lett.* **7**, 3603-3608 (2016)

[39] Li, Z. et al. Stabilizing perovskite structures by tuning tolerance factor: formation of formamidinium and cesium lead iodide solid-state alloys. *Chem. Mater.* **28**, 284-292 (2016)

[40] Zhu, W et al. Intermolecular exchange boosts efficiency of air-stable, carbon-based all-inorganic planar $CsPbIBr_2$ perovskite solar cells to over 9%. *Adv. Energy Mater.* **8**, 1802080 (2018)

[41] Yao, J. D. et al. Stable, highly-responsive and broadband photodetection based on large-area multilayered WS_2 films grown by pulsed-laser deposition. *Nanoscale* **7**, 14974-14981 (2015)

[42] Yu, J. et al. High-performance visible-blind ultraviolet photodetector based on IGZO TFT coupled with p–n heterojunction. *ACS Appl. Mater. Interfaces* **10**, 8102-8109 (2018)

Chapter 4 Robust long-term stability of all-inorganic orthorhombic black γ-$CsPbI_3$ perovskites with UV-curable polymer network

4.1 Overview

Halide perovskites are considered as the next generation optoelectronic materials because of excellent optoelectronic properties owing to inherent direct band gaps, high absorption coefficients, long exciton diffusion lengths, and low-cost solution process availabilities [1-3]. Among them, organic-inorganic hybrid perovskites in which organic cations such as methylammonium [4, 5] or formamidinium [6, 7] are applied to the position A of ABX_3 structure have been preferentially studied for realizing a cubic structure by satisfying the Goldschmidt tolerance factor ($0.81<t<1.1$, $t = (r_A + r_X)/\sqrt{2}(r_B + r_X)$, where r_A, r_B, and r_X are the ionic sizes of A, B, and X, respectively) [8, 9]. However, due to the inherent volatility problems of the organic cations [10, 11], all-inorganic perovskite ($CsPbX_3$, X = I, Br, Cl) which replaced the organic cation with cesium is drawing attention recently [12-17]. Particularly, in the case of $CsPbI_3$ in which the iodine is in the X position, it is intensively studied as a visible light detection material because it can effectively absorb the entire visible light [18-20].

In general, cubic α-$CsPbI_3$ (black phase) has suitable low bandgap (~1.70 eV) that can effectively absorb the visible region. Unfortunately, α-$CsPbI_3$ is unstable below 330 ℃ and undergoes rapid phase transition to undesirable large bandgap (~2.80 eV) orthorhombic δ-$CsPbI_3$ (yellow phase) at the room temperature [21]. Recently, adding hydroiodic acid (HI) enables lower formation energy of perovskite that is to realize relatively stable orthorhombic γ-$CsPbI_3$ (~1.69 eV, black phase) in a low-temperature process at about 100 ℃ [22-24]. However, there is still a challenge of phase transition occurrence to δ-$CsPbI_3$ upon prolonged exposure of γ-$CsPbI_3$ to ambient conditions.

To secure the long-term stability of the black phase $CsPbI_3$ under ambient conditions, two approaches have been developed: partial substitution of anion or cation [25-28], and surface passivation using organic additives [29-32]. One of the partial substitution methods, $CsPbI_nBr_{3-n}$ implemented by partially replacing bromide at the iodide position possesses wider bandgap than α and γ-$CsPbI_3$, thereby it is compromise way which is difficult to effectively absorb visible light [25]. The surface passivation method using organic additives, another approach to achieving improved stability, deteriorates the electrical properties of perovskite due to excess additives (10~70 wt% [29]) for realizing long-term stable black phase $CsPbI_3$.The above methods obviously provide a roadmap for $CsPbI_3$ to stabilize the

black phase in the long-term, but still contain the issues of bandgap widening and electrical properties deterioration.

In this chapter, I propose a robust strategy by employing infinitesimal (≤ 3 wt%) UV-curable oligo(ethylene glycol) dimethacrylate (OEGDMA) to ensure the structural and electrical long-term stability of the γ-$CsPbI_3$ under ambient conditions. Oxygen lone-pair electrons of the OEGDMA capture Cs^+ and Pb^{2+} cations and improve considerably the crystal growth of γ-$CsPbI_3$ around OEGDMA. Additionally, polymer network of OEGDMA processed by UV exposure, strongly contributes to maintaining the γ-$CsPbI_3$ structure tight for more than 35 days in ambient conditions. To evaluate the optoelectronic properties, two-terminal photoresistors were fabricated and evaluated, the optimized UV-cured γ-$CsPbI_3$ (3 wt% OEGDMA) film showed that ~90% of the initial electrical values responding to red, green, and blue lights, were stably maintained even after 35 days in the ambient conditions.

4.2 Feasibility of long-term stable perovskite $CsPbI_3$ by UV-curable polymer network

Figures 4.1-4.3 show the feasibility of long-term stabilized black phase $CsPbI_3$ under ambient conditions when UV is irradiated to thin film prepared by the spin coating method with $CsPbI_3$ precursor solution containing a small amount of OEGDMA with photo-initiator (2-Hydroxy-2-methylpropiophenone; HMPP). The reference $CsPbI_3$, and the $CsPbI_3$ with or without UV-curing after the addition of OEGDMA showed absorbance peaks from ~ 730 nm in the fresh state (Fig. 4.1a). As a result of recalculating the UV-vis spectroscopy analysis data and deriving the Tauc's plot, the optical bandgap of reference $CsPbI_3$ is 1.72 eV, and the $CsPbI_3$ with or without UV-curing after the addition of OEGDMA are 1.69 eV, that all samples exhibit black color to the naked eye (Fig 4.1c). After the above three $CsPbI_3$ samples were left in the air for 5 days, $CsPbI_3$ with or without UV-curing after adding OEGDMA maintained an optical bandgap of 1.69 eV. However, in the case of the reference $CsPbI_3$ without OEGDMA, an undesirable phase transition (yellow colored) occurred, which means that the optical bandgap derived to 2.82 eV. Even adding OEGDMA, the $CsPbI_3$ that did not undergo UV irradiation maintained a bandgap of 1.69 eV, but the phase transition is progressing slowly, and it shows slightly brown to the naked eye after 5 days (Fig. 4.1b, d). However, the $CsPbI_3$

with UV-curing after the addition of OEGDMA stably maintained a bandgap of 1.69 eV and the color of black even after 5 days. These results indicate that UV-cured OEGDMA network is a direct clue to keeping the perovskite's lattice structure firmly under atmospheric conditions. Using attenuated total reflection Fourier transform infrared (ATR-FTIR) spectroscopy, we measured the IR absorbance of OEGDMA before and after UV irradiation to investigate qualitatively for the conversion of C=C double bonds in the methacrylate group of OEGDMA (Fig. 4.2). Each OEGDMA has two methacrylate end groups, which, when exposed with UV, react with four other methacrylate groups through radical polymerization to make a covalent bond, and the OEGDMA forms a cross-linked network (Fig. 4.3) [33]. The C=C peak of the methacrylate group of OEGDMA disappeared completely after UV irradiation. In addition, as the C=C peak at 1637 cm^{-1} disappeared, the C=O peak was blue-shifted from 1716 cm^{-1} to 1722 cm^{-1} due to the C=C double bond being converted to a C-C single bond, so that is clear evidence the OEGDMA was fully UV-cured [34].

Through the XRD analysis, with the fresh state, the reference $CsPbI_3$, the $CsPbI_3$ with or without UV-curing after the addition of OEGDMA showed Bragg peaks at 14.16˚, 14.33˚, 28.54˚ and 28.89˚, which corresponded to the (200), (100), (400) and (220) planes of the orthorhombic γ-$CsPbI_3$ (Pbnm space group) crystallites,

respectively [20, 23]. However, after exposure to ambient condition for 7 days, the only $CsPbI_3$ with UV-cured OEGDMA network maintained stably the black γ-$CsPbI_3$ phase (Fig. 4.4).

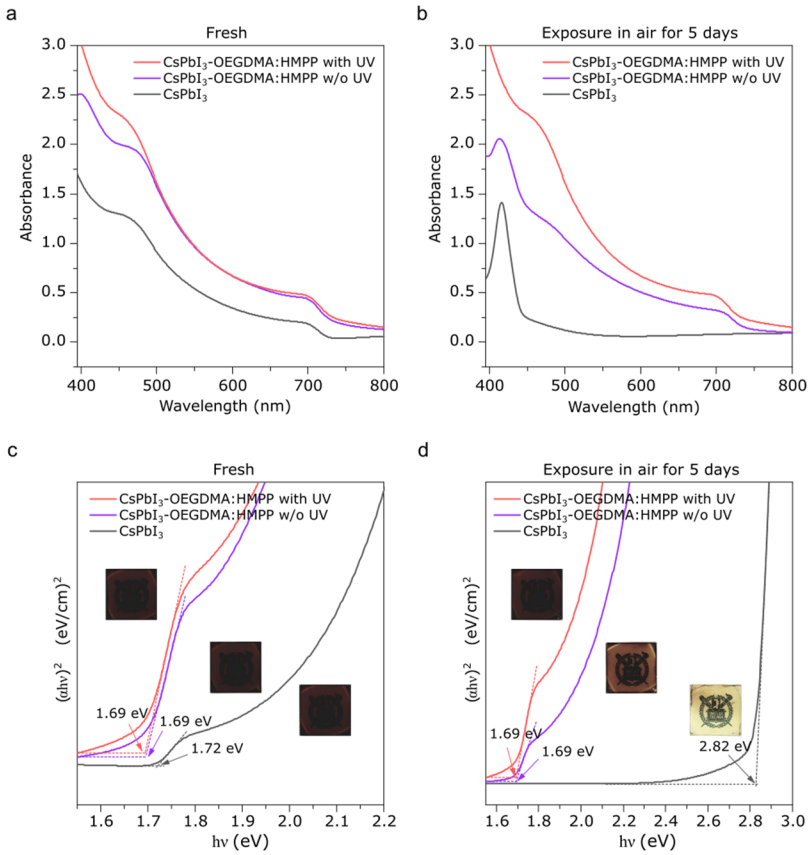

Figure 4. 1 Feasibility of long-term stable perovskite by UV-curable polymer network. a, b, The UV-vis spectrum of the reference $CsPbI_3$, and $CsPbI_3$ with or without UV-curing after the addition of OEGDMA, at the fresh state (a), and after 5 days left in the ambient conditions (b). c, d, Tauc's plot derived from the UV-vis spectroscopy analysis data of the fresh state (c), and after 5 days left in the ambient conditions (d). Inset: photographic images of the reference $CsPbI_3$, and $CsPbI_3$ with or without UV-curing after the addition of OEGDMA.

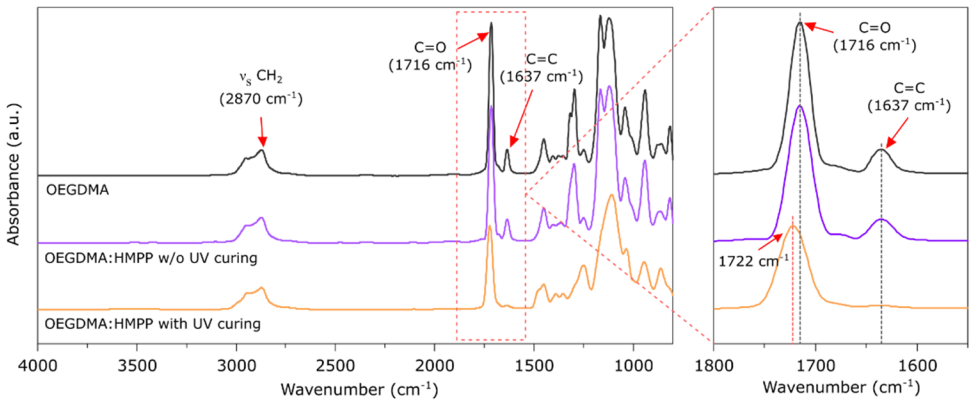

Figure 4. 2 ATR-FTIR spectroscopy analysis to investigate qualitatively for the conversion of C=C double bonds in the methacrylate group of OEGDMA whether UV irradiation.

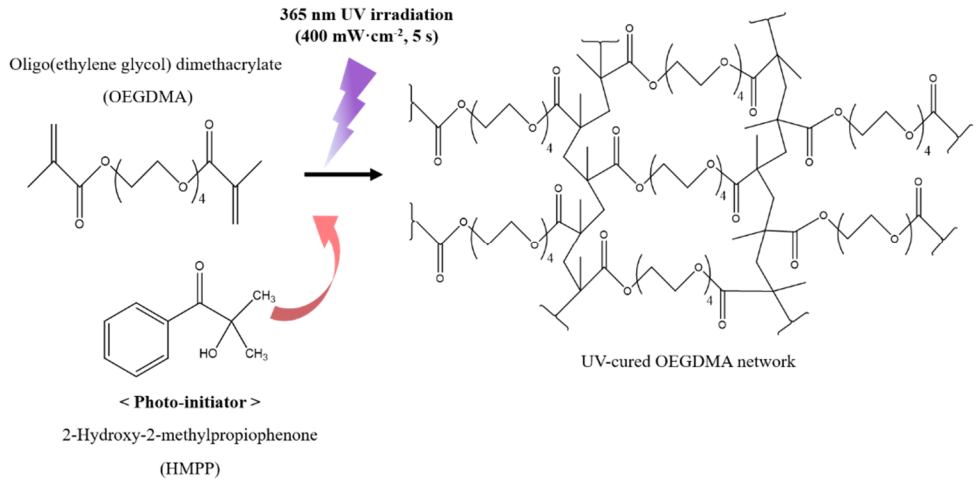

Figure 4. 3 UV-curing reaction mechanism of the OEGDMA. Each OEGDMA has two methacrylate end groups, which, when exposed with UV, react with four other methacrylate groups through radical polymerization to make a covalent bond, and the OEGDMA forms a cross-linked network.

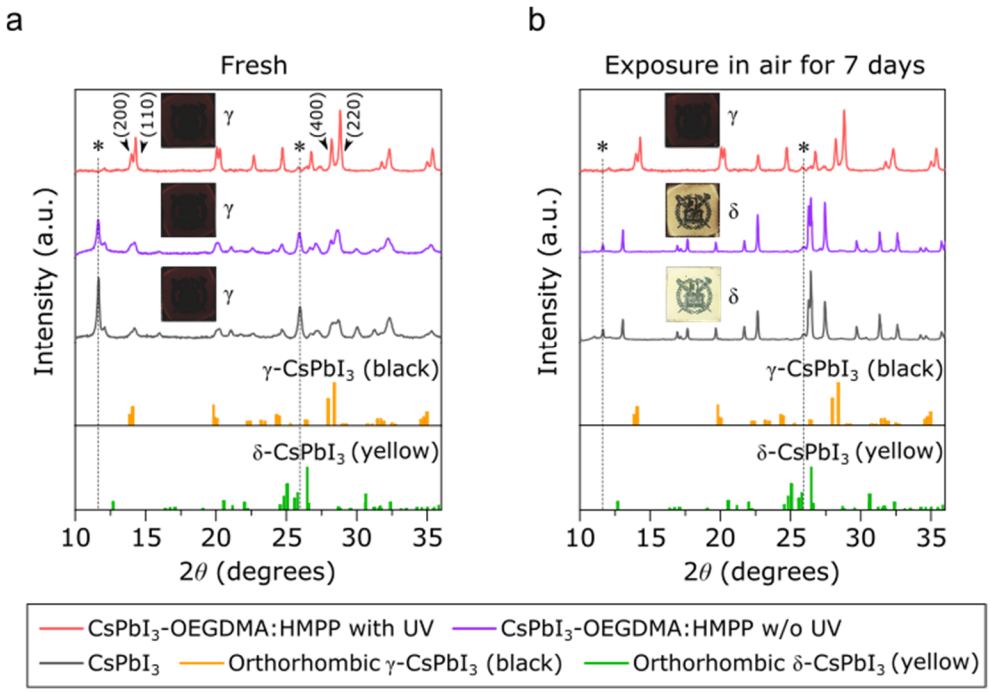

Figure 4. 4 XRD patterns of the reference $CsPbI_3$, and $CsPbI_3$ with or without UV-curing after the addition of OEGDMA, at the fresh state (a), and after 7 days left in the ambient conditions (b). Asterisk: $HPbI_{3+x}$ [20]

4.2.1 A conceivable mechanism for the introduction of the OEGDMA UV-curing strategy

In a previous study, Yin's group reported that the electronegative acylamino group of the poly-vinylpyrrolidone (PVP) molecule attracts the cation of the $CsPbI_3$ precursor to help the $CsPbI_3$ nucleus stably launch from around the PVP molecule [30]. Similarly, the acrylate group of OEGDMA also exhibits electronegative properties. The rich oxygen lone pair electrons of the acrylate group effectively attract Cs^+ and Pb^{2+} cations in the precursor solution to induce $CsPbI_3$ nuclei formation and crystal growth from the OEGDMA molecular backbone chain. The OEGDMA molecules prevent the aggregation of perovskite crystals grown in the precursor solution due to the intermolecular rejection effect [30, 32] of each other, and help to form a stable colloid (Fig. 4. 5a). After spin-coating process, the $CsPbI_3$ with OEGDMA annealed at 90 °C for 5 minutes and exposed UV for 5 seconds immediately before cooling, which induces to photopolymerization between OEGDMAs, thus $CsPbI_3$ crystals in the thin film were fixed more compactly without any extra byproducts (Fig. 4. 5b). Therefore, the OEGDMA induce $CsPbI_3$ nuclei formation and crystal growth from the OEGDMA molecular backbone chain, the γ-$CsPbI_3$ structure, which is tightly fixed by the UV-cured OEGDMA polymer network, can maintain the robust γ-phase under ambient conditions (Fig. 4. 5c).

Furthermore, dynamic light scattering (DLS) analysis was performed to confirm whether the rich oxygen lone pair electrons of the acrylate group effectively attract Cs^{+} and Pb^{2+} cations in the precursor solution to induce $CsPbI_3$ nuclei formation and crystal growth from the OEGDMA molecular backbone chain. (Fig. 4.6) It was confirmed that the colloid size of $CsPbI_3$ (0 wt% OEGDMA) precursor solution was containing monodispersed $CsPbI_3$ crystal having a diameter of 1.32 nm. However, as the content of OEGDMA increased from 0.5 to 5 wt%, additional satellite peak was observed, unlike the $CsPbI_3$ (0 wt% OEGDMA) solution. As the content of OEGDMA increased, the intensity of the $CsPbI_3$ crystal colloid gradually decreased, and on the contrary, the intensity of the satellite peak increased and the corresponding colloid size also increased to 173.09, 428.47, 614.62, and 1319.97 nm, respectively. Consequently, the fact that the observed colloid size is clearly distinguished as the amount of OEGDMA added increases means that OEGDMA induces $CsPbI_3$ nuclear growth and directly affects crystal growth. Therefore, this result is strong evidence supporting Fig. 4.5a.

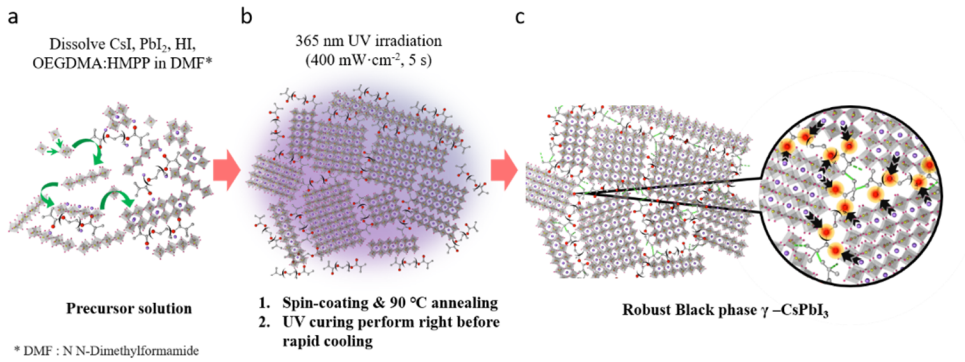

Figure 4. 5 A conceivable mechanism for the introduction of the OEGDMA UV-curing strategy to improve the long-term stability of $CsPbI_3$. a, Step 1: Induced $CsPbI_3$ nuclei formation and crystal growth from the OEGDMA molecular backbone chain by the OEGDMA's oxygen lone pair electrons in the precursor solution. b, Step 2: UV-curing process immediately before cooling, on the spin-coated and annealed $CsPbI_3$ after the addition of OEGDMA. UV irradiation: 365nm, 400 $mW \cdot cm^{-2}$ for 5 seconds. c, Step 3: Establishment of the robust γ-$CspbI_3$ with the UV-cured OEGDMA polymer network.

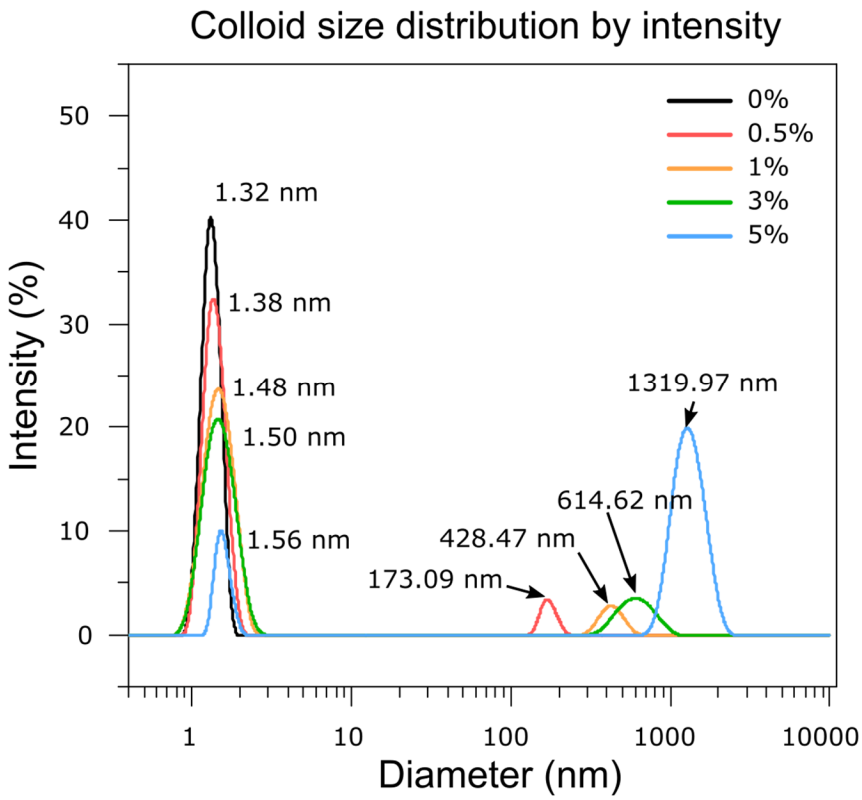

Figure 4. 6 DLS analysis for $CsPbI_3$ precursor solution containing with different amounts of OEGDMA (0, 0.5, 1, 3, 5 wt%).

4.3 The correlation between OEGDMA content and black γ-$CsPbI_3$ optical long-term stability

I investigated in-depth the effect of the content of UV-cured OEGDMA polymer network inside $CsPbI_3$ thin film on the atmospheric stability of γ-$CsPbI_3$. Figures 4. 7-4. 10 show the effect on the optical long-term stability of γ-$CsPbI_3$ by splitting the OEGDMA content added to the $CsPbI_3$ precursor solution into 0, 0.5, 1, 3, and 5 wt%, respectively. For convenience, the group of γ-$CsPbI_3$ thin-film samples with adding different wt% of OEGDMA cured by UV after spin coating are briefly referred to as γ-$CsPbI_3$ (0, 0.5, 1, 3, and 5 wt% OEGDMA), respectively. Fig. 4. 7 a-e is the result of accumulating UV-vis absorbance spectra while exposing γ-$CsPbI_3$ (0, 0.5, 1, 3, and 5 wt% OEGDMA) to the ambient conditions for 35 days. The variation of optical property of γ-$CsPbI_3$ (0, 0.5, 1, 3, and 5 wt% OEGDMA) for 35 days were measured at ambient conditions with 20.50 ± 1.10 °C for temperature and 26.81 ± 2.56 % for relative humidity, respectively. (Fig. 4. 8 and Table 4. 1, 4. 2). The γ-$CsPbI_3$ (0 wt% OEGDMA) was rapidly changed to δ-$CsPbI_3$ as the phase transition began 3 days after exposure to the ambient conditions, but γ-$CsPbI_3$ (0.5, 1, 3, and 5 wt% OEGDMA) were kept stable black phase in the long term as the OEGDMA content increased. Specially, both γ-$CsPbI_3$ (3 wt% OEGDMA) and γ-$CsPbI_3$ (5 wt% OEGDMA), even after 35 days after exposure to

the ambient conditions, the absorbance peak was stably observed at ~730 nm, and the spectrum change was almost negligible. Interestingly, as the OEGDMA content increased, the absorbance peak intensity at the 720 nm position of all fresh γ-$CsPbI_3$ (0, 0.5, 1, 3, and 5 wt% OEGDMA) follows a linear relationship with the OEGDMA content (Fig. 4. 9). This means that OEGDMA directly affects the growth of perovskite grain, and this tendency is clearly confirmed through the field emission scanning electron microscopy (FE-SEM) images in Fig. 4. 10.

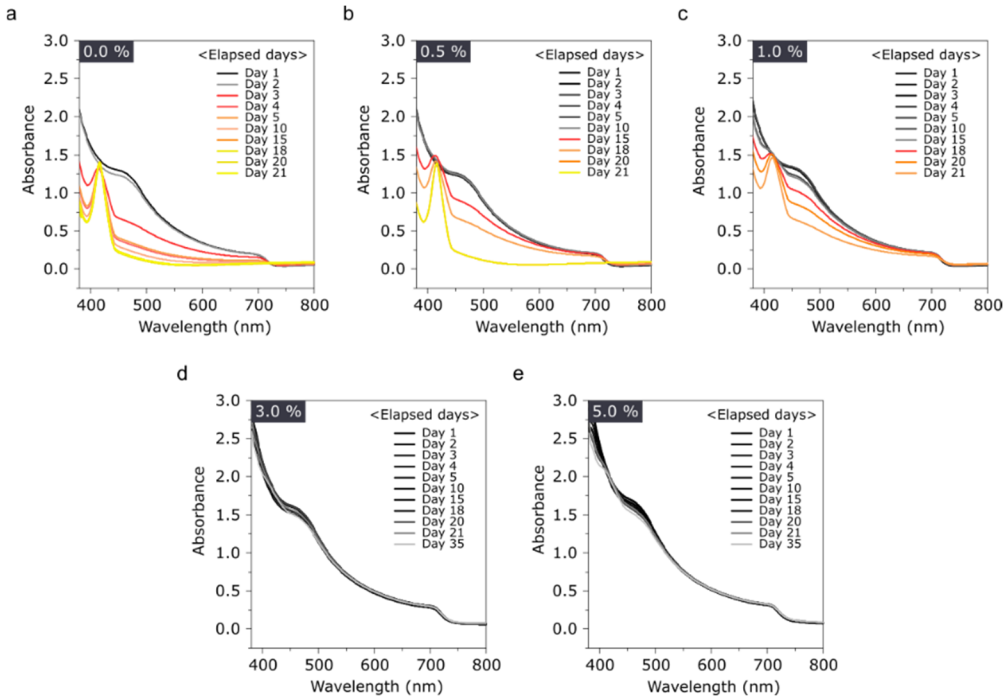

Figure 4. 7 a-e, Accumulated UV-vis absorbance spectra while exposing γ-$CsPbI_3$ (0, 0.5, 1, 3, and 5 wt% OEGDMA) to the ambient conditions for 35 days.

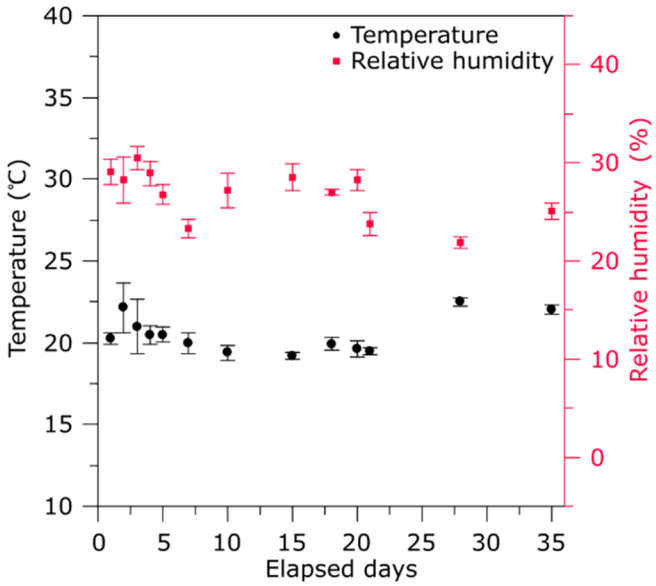

Figure 4. 8 Ambient conditions where γ-$CsPbI_3$ (0, 0.5, 1, 3, and 5 wt% OEGDMA) stored for 35 days. The ambient conditions measured with 20.50 ± 1.10 °C for temperature and 26.81 ± 2.56 % for relative humidity, respectively for 35 days.

Days	Temperature with different measuring time (℃)					Average (℃)
	AM 09:00	PM 12:00	PM 14:00	PM 18:00	PM 22:00	
1	20.2	19.9	20.4	20.8	20.0	20.26 ± 0.36
2	22.5	21.8	24.1	22.5	19.9	22.16 ± 1.52
3	19.4	20.2	22.5	23.0	19.8	20.98 ± 1.65
4	20.5	20.8	21.2	19.9	20.0	20.48 ± 0.54
5	20.2	21.0	20.9	20.5	19.9	20.50 ± 0.46
7	19.8	19.4	19.4	20.5	20.8	19.98 ± 0.64
10	19.5	19.2	19.1	20.1	19.0	19.38 ± 0.44
15	19.1	19.3	19.2	18.9	19.5	19.20 ± 0.22
18	19.4	19.9	20.5	20.1	19.8	19.94 ± 0.40
20	20.2	19.9	19.5	18.9	19.5	19.60 ± 0.49
21	19.3	19.4	19.6	19.8	19.4	19.50 ± 0.20
28	22.1	22.5	22.7	22.7	22.5	22.50 ± 0.24
35	21.8	22.0	22.4	22.3	21.7	22.04 ± 0.30

Table 4. 1 The variation of the ambient temperature for 35 days.

Days	Relative humidity with different measuring time (%)					Average (%)
	AM 09:00	PM 12:00	PM 14:00	PM 18:00	PM 22:00	
1	30.2	29.8	30.1	27.4	28.1	29.12 ± 1.28
2	31.4	29.7	28.1	26.5	25.6	28.26 ± 2.35
3	29.5	31.0	32.2	30.4	29.4	30.50 ± 1.16
4	28.6	28.8	30.4	29.6	27.2	28.92 ± 1.19
5	26.8	28.0	27.2	26.8	25.1	26.78 ± 1.06
7	23.9	23.8	24.1	22.9	21.9	23.32 ± 0.92
10	27.4	29.0	28.7	26.3	24.6	27.20 ± 1.81
15	28.3	29.5	30.0	26.5	28.4	28.54 ± 1.35
18	26.7	27.4	27.1	26.9	26.7	26.96 ± 0.29
20	27.9	28.5	26.8	28.1	29.8	28.22 ± 1.08
21	22.4	23.1	23.6	25.2	24.6	23.78 ± 1.13
28	22.8	22.1	21.9	21.3	21.5	21.92 ± 0.58
35	25.5	25.7	25.8	24.4	23.9	25.06 ± 0.86

Table 4. 2 The variation of the ambient relative humidity for 35 days.

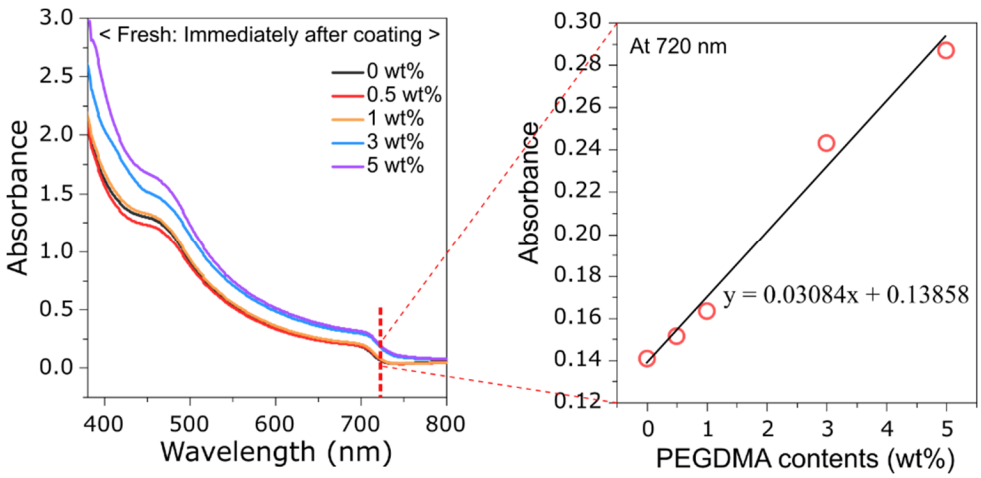

Figure 4. 9 A linear relationship with the OEGDMA content and the γ-$CsPbI_3$ (0, 0.5, 1, 3, and 5 wt% OEGDMA) absorbance peak intensity at the 720nm position.

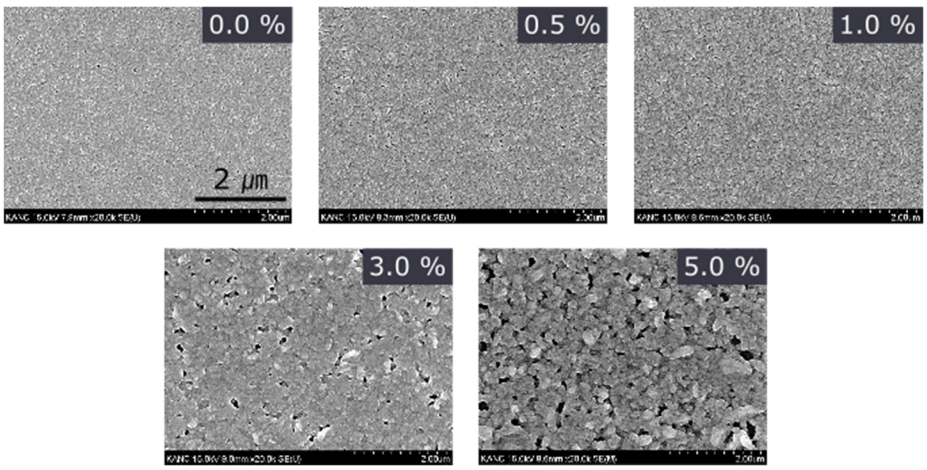

Figure 4. 10 FE-SEM top view images of γ-$CsPbI_3$ (0, 0.5, 1, 3, and 5 wt% OEGDMA). Scale bar: 2 μm.

Fig. 4. 11 shows the time-dependent photographic results obtained by observing the optical color change of the γ-$CsPbI_3$ (0, 0.5, 1, 3, and 5 wt% OEGDMA) thin films, which were continuously exposed to the ambient conditions. The red square box represents the limitation of γ-phase stability that begins to transition from the γ-phase to the δ-phase, which perfectly matches the UV-vis spectral trend of Fig. 4. 7a-e. The XPS analysis was performed on the fresh γ-$CsPbI_3$ (0, 0.5, 1, 3, and 5 wt% OEGDMA) to confirm the $CsPbI_3$ lattice binding energy varying with OEGDMA content (Fig. 4. 12a-d). In case of pure γ-$CsPbI_3$ (0 wt% OEGDMA), the Cs 3d spectra show two peaks at 723.5 and 737.2 eV corresponding to the binding energies of Cs $3d_{5/2}$ and Cs $3d_{3/2}$, respectively. The Pb 4f spectra show two peaks at 137.6 and 142.5 eV corresponding to the binding energies of Pb $4f_{7/2}$ and Pb $4f_{5/2}$, and the spectra of I 3d also exhibit two peaks at 618 and 629.3 eV corresponding to I $3d_{5/2}$ and I $3d_{3/2}$, respectively. However, in cases of γ-$CsPbI_3$ (0.5, 1, 3, and 5 wt% OEGDMA), as the OEGDMA content increased, Cs 3d and Pb 4f binding energy were significantly lowered by 0.7 eV, and I 3d was also slightly shifted to the low binding energy. Therefore, as the OEGDMA content increases, the oxygen lone pair sites also increase linearly, so the binding energy of Cs 3d and Pb 4f peaks are lowered by causing a stronger interaction between the cations of the γ-$CsPbI_3$ and oxygen lone pairs of OEGDMA. Since the binding energy of Cs^+ and Pb^{2+} ions

forming the γ-$CsPbI_3$ lattice was lowered, the anion I 3d peaks were also shifted slightly to the lower binding energy as a side effect. Consequently, XPS analysis results provide strong evidence supporting the mechanism by which the electronegative oxygen lone pair of OEGDMA shown in Fig. 4. 5 attracts Cs^+ and Pb^{2+} ions of $CsPbI_3$.

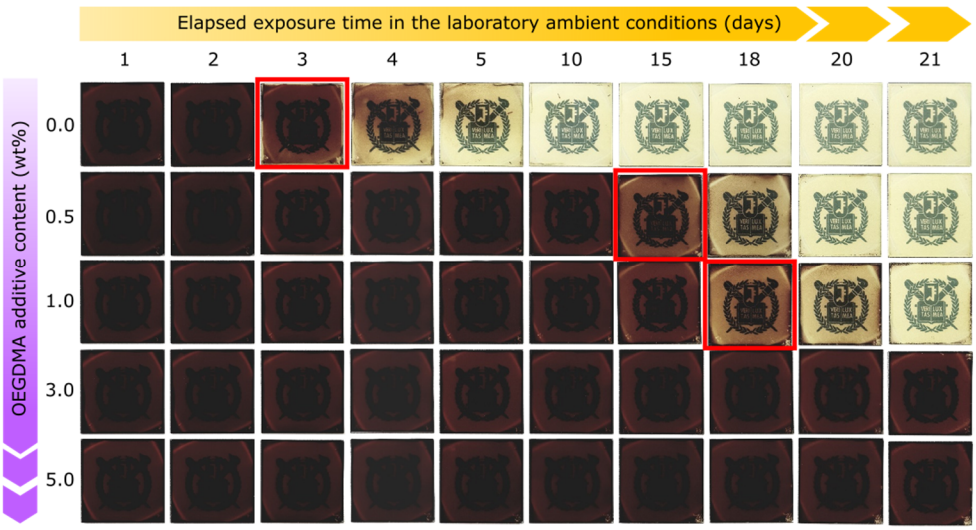

Figure 4. 11 Time-dependent photographic results obtained by observing the optical color change of the γ-$CsPbI_3$ (0, 0.5, 1, 3, and 5 wt% OEGDMA) thin films during 35 days in ambient conditions. The red square box represents the limitation of γ-phase stability that begins to transition from the γ-phase to the δ-phase.

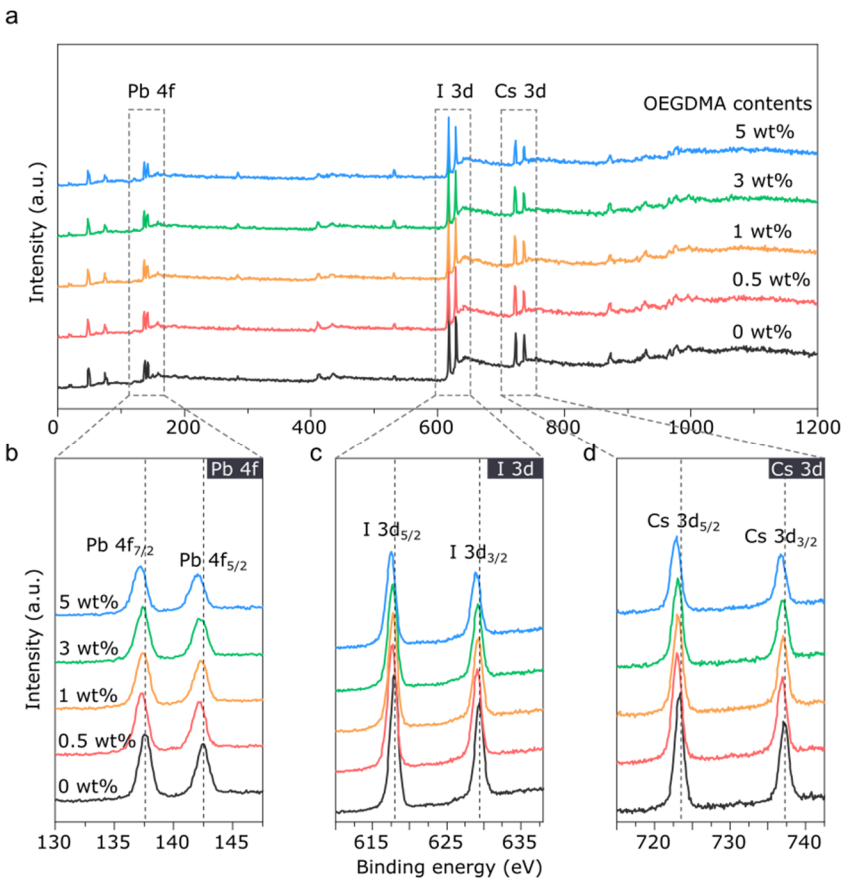

Figure 4. 12 XPS analysis on the fresh γ-$CsPbI_3$ (0, 0.5, 1, 3, and 5 wt% OEGDMA) at full range (a), Pb 4f (b), I 3d (c), and Cs 3d (d).

4.4 Optoelectrical properties and stabilities variation according to the OEGDMA polymer network content in γ-$CsPbI_3$

To confirm the applicability of γ-$CsPbI_3$ with OEGDMA polymer network as a light detecting material, 2-terminal lateral photoresistors with channel length and width of 120 um, 1000 um, respectively, were fabricated in Au/γ-$CsPbI_3$ (0, 0.5, 1, 3, and 5 wt% OEGDMA)/Au structure. Figure 4. 13 shows the electrical properties of photoresistor under irradiation of 0.4 mW $\cdot cm^{-2}$ of red (635 nm), green (532 nm), and blue (450 nm) LED light sources. Fig. 4. 12a-e represent the photoresponse I-V characteristics of photoresistors including γ-$CsPbI_3$ (0, 0.5, 1, 3, and 5 wt% OEGDMA). As the OEGDMA content increased, the dark current of the γ-$CsPbI_3$ (0, 0.5, 1, 3, and 5 wt% OEGDMA) device decreased. The dark current of the γ-$CsPbI_3$ (0 wt% OEGDMA) device showed a relatively large value of 8.0×10^{-10} A, while the γ-$CsPbI_3$ (5 wt% OEGDMA) device slightly decreased by 6.47×10^{-11} A. On the other hand, when red, green, and blue light was irradiated, the photocurrent of photoresistors including the γ-$CsPbI_3$ (0, 0.5, 1, and 3 wt% OEGDMA) tended to increase as the increment of PEGDMA content from 0 wt% to 3 wt%. As mentioned in Fig. 4. 6 and 4. 10, the increment of PEGDMA content attributes to the large growth of perovskite grains and within such large grains, charge carriers

generally exhibit a longer mean free-path which would yield a higher photocurrent. However, the photocurrent of γ-$CsPbI_3$ (5 wt% OEGDMA) did not follow the above trend. Since the γ-$CsPbI_3$ grains, irregularly overgrown when 5 wt% OEGDMA was added, the film exhibits poor roughness which hinders the charge carrier transport from the $CsPbI_3$ to the electrodes. In addition, the 5wt% OEGDMA-added film suppresses the generation of effective photocurrent because it contains a large number of pinholes that cause scattering of photogenerated charge carriers. As a result of measuring the I-V curve after continuously exposing these devices to the ambient conditions for 35 days, γ-$CsPbI_3$ (3 wt% OEGDMA) device showed ~90% of photoelectrical performance compared to the initial state (Fig. 4. 14 and Table 4. 3). Figs. 4. 15 a, b show the comparison of additional optical response parameters between as-prepared and after 35 days of Au/γ-$CsPbI_3$ (0, 0.5, 1, 3, and 5 wt% OEGDMA)/Au photoresistors. To determine whether $CsPbI_3$ with UV-cured OEGDMA network continuously maintains the black phase and the photoelectric properties, we tested the response of the photoresistor on red-colored (635 nm) light in cases of fresh and 35 days, respectively (Table 4. 4).

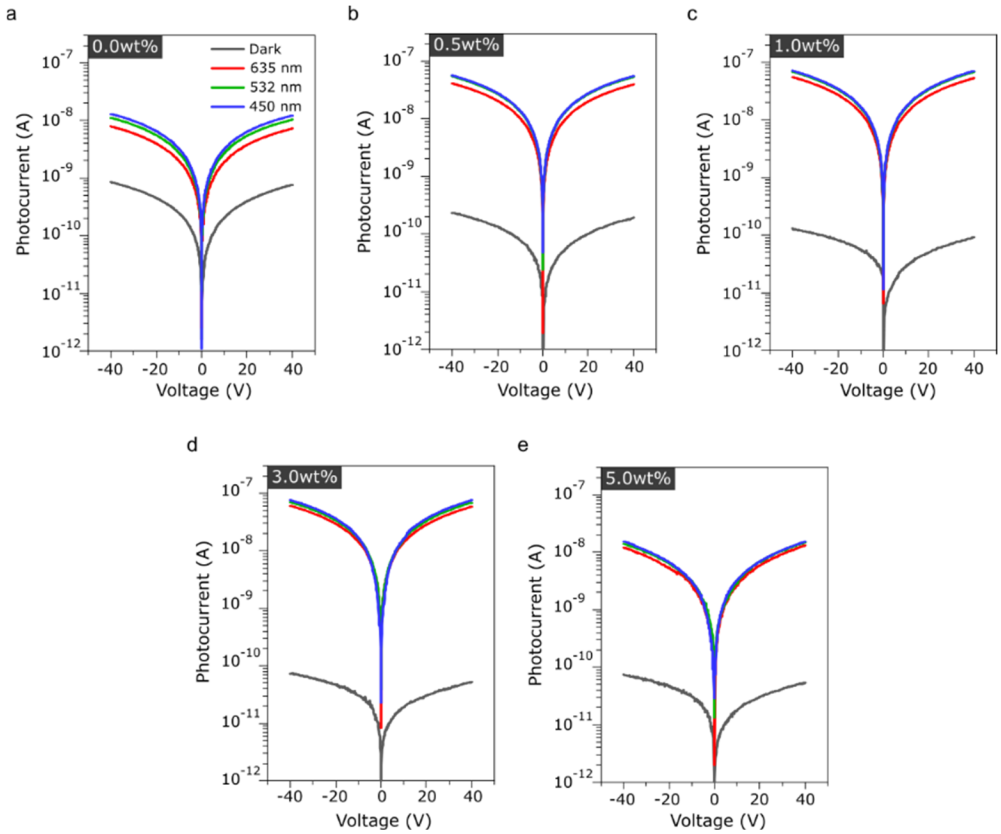

Figure 4. 13 a-e, Photoresponse I-V characteristics of photoresistors including fresh γ-$CsPbI_3$ (0, 0.5, 1, 3, and 5 wt% OEGDMA), under irradiation of 0.4 mW ·cm^{-2} of red (635 nm), green (532 nm), and blue (450 nm) LED light sources.

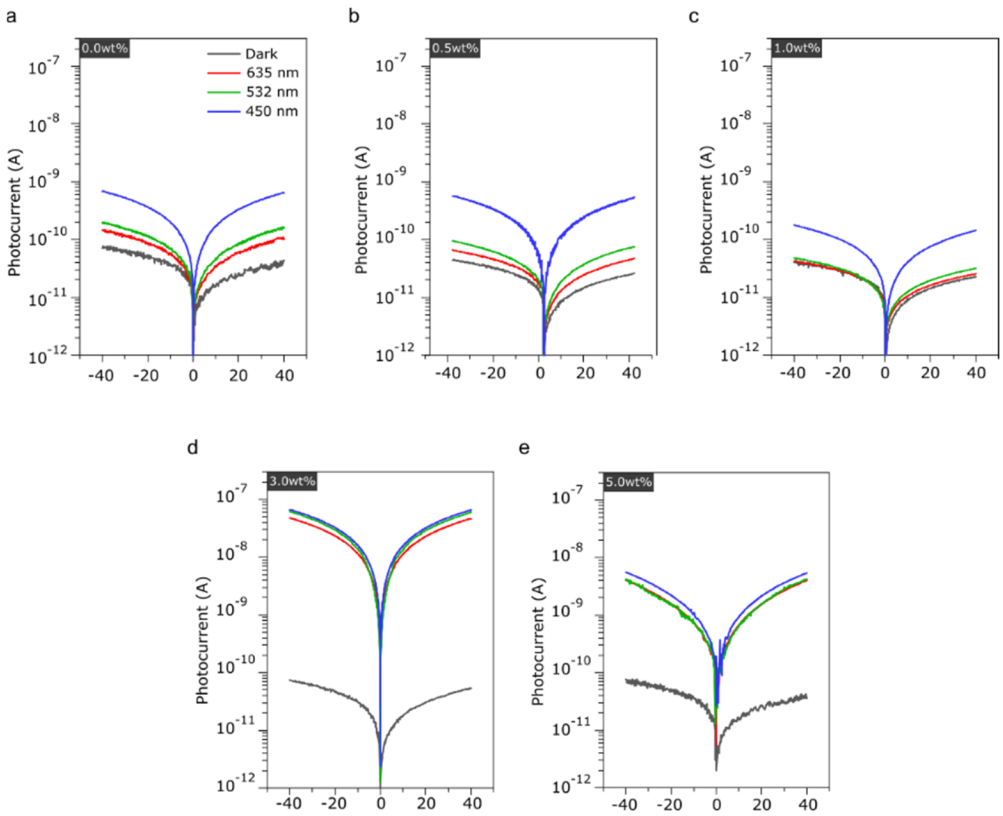

Figure 4. 14 a-e, Photoresponse I-V characteristics of photoresistors including 35 days elapsed γ-$CsPbI_3$ (0, 0.5, 1, 3, and 5 wt% OEGDMA), under irradiation of 0.4 mW $\cdot cm^{-2}$ of red (635 nm), green (532 nm), and blue (450 nm) LED light sources.

		Fresh				Elapsed			
OEGDMA contents (wt%)	Wavelength (nm)	I_{photo}/I_{dark}	R (A/W)	EQE (%)	D^* (Jones)	I_{photo}/I_{dark}	R (A/W)	EQE (%)	D^* (Jones)
0 %	635 nm	9.05×10^{0} $\pm 1.63 \times 10^{0}$	1.50×10^{-2} $\pm 2.55 \times 10^{-3}$	2.61×10^{0} $\pm 4.67 \times 10^{-1}$	3.26×10^{10} $\pm 5.59 \times 10^{9}$	1.92×10^{0} $\pm 9.78 \times 10^{-2}$	2.83×10^{-4} $\pm 2.65 \times 10^{-5}$	2.64×10^{-2} $\pm 3.33 \times 10^{-3}$	2.06×10^{9} $\pm 1.28 \times 10^{8}$
	532 nm	1.30×10^{1} $\pm 4.92 \times 10^{-2}$	2.17×10^{-2} $\pm 1.39 \times 10^{-3}$	4.67×10^{0} $\pm 3.01 \times 10^{-1}$	4.70×10^{10} $\pm 1.54 \times 10^{9}$	2.65×10^{0} $\pm 8.23 \times 10^{-2}$	3.91×10^{-4} $\pm 3.73 \times 10^{-5}$	5.68×10^{-2} $\pm 5.90 \times 10^{-3}$	2.85×10^{9} $\pm 1.60 \times 10^{8}$
	450 nm	1.52×10^{1} $\pm 1.10 \times 10^{0}$	2.52×10^{-2} $\pm 1.94 \times 10^{-3}$	6.50×10^{0} $\pm 5.21 \times 10^{-1}$	5.47×10^{10} $\pm 3.66 \times 10^{9}$	9.54×10^{0} $\pm 4.35 \times 10^{-1}$	1.40×10^{-3} $\pm 6.27 \times 10^{-5}$	3.46×10^{-1} $\pm 1.38 \times 10^{-2}$	1.02×10^{10} $\pm 8.98 \times 10^{7}$
0.5 wt%	635 nm	2.00×10^{2} $\pm 2.26 \times 10^{1}$	7.78×10^{-2} $\pm 1.02 \times 10^{-2}$	1.51×10^{1} $\pm 1.97 \times 10^{0}$	3.47×10^{11} $\pm 1.37 \times 10^{10}$	1.49×10^{0} $\pm 8.96 \times 10^{-2}$	1.30×10^{-4} $\pm 9.03 \times 10^{-6}$	1.55×10^{0} $\pm 9.86 \times 10^{-2}$	9.43×10^{8} $\pm 2.22 \times 10^{7}$
	532 nm	2.67×10^{2} $\pm 3.02 \times 10^{1}$	1.04×10^{-1} $\pm 1.43 \times 10^{-2}$	2.41×10^{1} $\pm 3.30 \times 10^{0}$	4.63×10^{11} $\pm 2.45 \times 10^{10}$	2.15×10^{0} $\pm 9.63 \times 10^{-2}$	1.88×10^{-4} $\pm 1.57 \times 10^{-5}$	1.93×10^{0} $\pm 1.64 \times 10^{-1}$	1.78×10^{9} $\pm 4.72 \times 10^{7}$
	450 nm	2.79×10^{2} $\pm 3.51 \times 10^{1}$	1.08×10^{-1} $\pm 1.31 \times 10^{-2}$	2.98×10^{1} $\pm 3.58 \times 10^{0}$	4.84×10^{11} $\pm 2.04 \times 10^{10}$	1.34×10^{1} $\pm 1.39 \times 10^{0}$	1.16×10^{-3} $\pm 2.99 \times 10^{-5}$	2.96×10^{-1} $\pm 5.46 \times 10^{-3}$	1.10×10^{10} $\pm 4.25 \times 10^{8}$
1 wt%	635 nm	4.78×10^{2} $\pm 8.69 \times 10^{1}$	1.08×10^{-1} $\pm 8.01 \times 10^{-3}$	2.11×10^{1} $\pm 1.56 \times 10^{0}$	6.34×10^{11} $\pm 6.56 \times 10^{10}$	1.07×10^{0} $\pm 2.34 \times 10^{-2}$	8.66×10^{-5} $\pm 3.59 \times 10^{-6}$	1.13×10^{-3} $\pm 3.41 \times 10^{-4}$	8.51×10^{8} $\pm 1.78 \times 10^{7}$
	532 nm	6.09×10^{2} $\pm 1.17 \times 10^{2}$	1.38×10^{-1} $\pm 8.04 \times 10^{-3}$	3.21×10^{1} $\pm 1.87 \times 10^{0}$	8.07×10^{11} $\pm 8.76 \times 10^{10}$	1.22×10^{0} $\pm 1.03 \times 10^{-1}$	9.84×10^{-5} $\pm 3.94 \times 10^{-6}$	4.10×10^{-3} $\pm 1.70 \times 10^{-3}$	9.68×10^{8} $\pm 5.83 \times 10^{7}$
	450 nm	6.40×10^{2} $\pm 1.16 \times 10^{2}$	1.45×10^{-1} $\pm 5.26 \times 10^{-3}$	3.98×10^{1} $\pm 1.45 \times 10^{0}$	8.49×10^{11} $\pm 8.17 \times 10^{10}$	4.53×10^{0} $\pm 2.67 \times 10^{-1}$	3.65×10^{-4} $\pm 2.44 \times 10^{-6}$	7.83×10^{-2} $\pm 1.75 \times 10^{-3}$	3.59×10^{9} $\pm 1.16 \times 10^{8}$
3 wt%	635 nm	9.07×10^{2} $\pm 3.92 \times 10^{1}$	1.22×10^{-1} $\pm 4.05 \times 10^{-3}$	2.38×10^{1} $\pm 7.88 \times 10^{-1}$	9.30×10^{11} $\pm 1.21 \times 10^{10}$	7.55×10^{2} $\pm 1.14 \times 10^{2}$	9.74×10^{-2} $\pm 2.09 \times 10^{-3}$	1.90×10^{1} $\pm 4.10 \times 10^{-1}$	7.56×10^{11} $\pm 5.94 \times 10^{10}$
	532 nm	1.08×10^{3} $\pm 7.00 \times 10^{1}$	1.45×10^{-1} $\pm 2.15 \times 10^{-3}$	3.37×10^{1} $\pm 4.99 \times 10^{-1}$	1.10×10^{12} $\pm 3.39 \times 10^{10}$	9.72×10^{2} $\pm 1.45 \times 10^{2}$	1.25×10^{-1} $\pm 2.90 \times 10^{-3}$	2.92×10^{1} $\pm 6.77 \times 10^{-1}$	9.74×10^{11} $\pm 7.53 \times 10^{10}$
	450 nm	1.18×10^{3} $\pm 7.91 \times 10^{1}$	1.59×10^{-1} $\pm 9.21 \times 10^{-4}$	4.36×10^{1} $\pm 2.51 \times 10^{-1}$	1.21×10^{12} $\pm 3.81 \times 10^{10}$	1.05×10^{3} $\pm 1.62 \times 10^{2}$	1.36×10^{-1} $\pm 2.93 \times 10^{-3}$	3.74×10^{1} $\pm 8.09 \times 10^{-1}$	1.06×10^{12} $\pm 8.55 \times 10^{10}$
5 wt%	635 nm	1.59×10^{2} $\pm 5.06 \times 10^{1}$	2.51×10^{-2} $\pm 2.40 \times 10^{-3}$	4.86×10^{0} $\pm 4.76 \times 10^{-1}$	1.76×10^{11} $\pm 3.68 \times 10^{10}$	5.50×10^{1} $\pm 2.30 \times 10^{1}$	8.11×10^{-3} $\pm 5.18 \times 10^{-4}$	1.55×10^{0} $\pm 9.86 \times 10^{-2}$	5.90×10^{10} $\pm 1.39 \times 10^{9}$
	532 nm	1.78×10^{2} $\pm 6.31 \times 10^{1}$	2.80×10^{-2} $\pm 4.10 \times 10^{-3}$	6.48×10^{0} $\pm 9.65 \times 10^{-1}$	1.97×10^{11} $\pm 4.97 \times 10^{10}$	5.71×10^{1} $\pm 1.78 \times 10^{1}$	8.43×10^{-3} $\pm 7.17 \times 10^{-4}$	1.93×10^{0} $\pm 1.64 \times 10^{-1}$	6.13×10^{10} $\pm 2.62 \times 10^{9}$
	450 nm	1.91×10^{2} $\pm 6.01 \times 10^{1}$	3.01×10^{-2} $\pm 3.39 \times 10^{-3}$	8.26×10^{0} $\pm 9.44 \times 10^{-1}$	2.11×10^{11} $\pm 4.52 \times 10^{10}$	7.47×10^{1} $\pm 3.15 \times 10^{1}$	1.10×10^{-2} $\pm 6.26 \times 10^{-4}$	2.99×10^{0} $\pm 1.68 \times 10^{-1}$	8.01×10^{10} $\pm 6.22 \times 10^{8}$

Table 4. 3 Comparison of additional optical response parameters between as-prepared and after 35 days of Au/γ-$CsPbI_3$ (0, 0.5, 1, 3, and 5 wt% OEGDMA)/Au photoresistors.

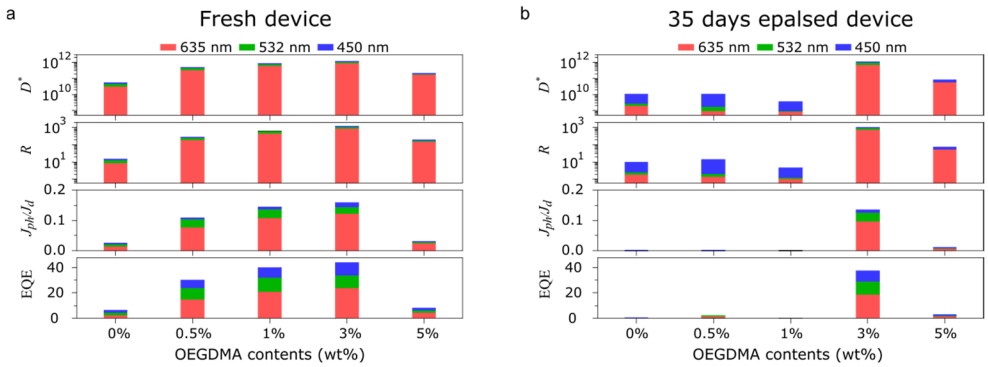

Figure 4. 15 The comparison of additional optical response parameters between as-prepared (a) and after 35 days (b) of Au/γ-$CsPbI_3$ (0, 0.5, 1, 3, and 5 wt% OEGDMA)/Au photoresistors. Unit of the parameters: *EQE* (%), J_{photo}/J_{dark}, *R* (A/W), *D** (Jones).

(At 635 nm)	Fresh				Elapsed			
OEGDMA contents (wt%)	I_{photo}/I_{dark}	*R* (A/W)	*EQE* (%)	*D** (Jones)	I_{photo}/I_{dark}	*R* (A/W)	*EQE* (%)	*D** (Jones)
0 %	9.05×10^{0} $\pm 1.63 \times 10^{0}$	1.50×10^{-2} $\pm 2.55 \times 10^{-3}$	2.61×10^{0} $\pm 4.67 \times 10^{-1}$	3.26×10^{10} $\pm 5.59 \times 10^{9}$	1.92×10^{0} $\pm 9.78 \times 10^{-2}$	2.83×10^{-4} $\pm 2.65 \times 10^{-5}$	2.64×10^{-2} $\pm 3.33 \times 10^{-3}$	2.06×10^{9} $\pm 1.28 \times 10^{8}$
3 wt%	9.07×10^{2} $\pm 3.92 \times 10^{1}$	1.22×10^{-1} $\pm 4.05 \times 10^{-3}$	2.38×10^{1} $\pm 7.88 \times 10^{-1}$	9.30×10^{11} $\pm 1.21 \times 10^{10}$	7.55×10^{2} $\pm 1.14 \times 10^{2}$	9.74×10^{-2} $\pm 2.09 \times 10^{-3}$	1.90×10^{1} $\pm 4.10 \times 10^{-1}$	7.56×10^{11} $\pm 5.94 \times 10^{10}$

Table 4. 4 Comparison of additional optical response parameters between fresh and after 35 days of Au/γ-$CsPbI_3$ (0, and 3 wt% OEGDMA)/Au photoresistors.

The γ-$CsPbI_3$ (3 wt% OEGDMA) device showed stable photo response characteristics in light of 635 nm as well as 450 and 532 nm even after exposure to ambient conditions for 35 days. The initial J_{photo}/J_{dark} of the γ-$CsPbI_3$ (3 wt% OEGDMA) device for 635nm light is 9.07×10^2, and the J_{photo}/J_{dark} after 35 days is 7.55×10^2. Initial Responsivity (R) is 0.122 A/W, and the responsivity after 35 days is 0.0974 A/W. In addition, normalized detectivity (D *) showed a value of 7.56×10^{11} Jones after 35 days from the initial value of 9.30×10^{11} Jones. The initial value of the external quantum efficiency (EQE) is 23.8 %, and the EQE after 35 days still retains 19 %, which shows excellent electrical long-term stability. Furthermore, to evaluate the repetitive driving stability of the optimized γ-$CsPbI_3$ (3 wt% OEGDMA) photoresistor, we measured the time-resolved photoresponse and transient response time (Figure 4. 16 and 4. 17). Photocurrent–time response was measured at 40 V applied bias in the dark and under illumination using the LEDs at 635 nm, 532nm, 450nm with fixed light intensity (P_{in} = 0.4 $mW \cdot cm^{-2}$) and frequency (1 Hz) (Fig. 4. 16a-d). Unlike the reference γ-$CsPbI_3$ (Fig. 4. 16a, b), the γ-$CsPbI_3$ (3 wt% OEGDMA) photoresistor showed stable and consistent repetitive driving characteristics not only the fresh state but also after 35 days (Fig. 4. 16c, d), and the photocurrent values were also matched with Fig. 4. 13d and Fig. 4. 14d. In addition, rise times in response to red, green, and blue light of fresh γ-$CsPbI_3$ (3 wt%

OEGDMA) were 65.1, 66.0, and 66.4 ms, and fall times were 66.8, 66.8, and 66.7 ms, respectively. Even after 35 days exposed in the ambient conditions, it shows an excellent fast response time that did not change much from the rise and fall time values of initial device (Fig. 4. 17).

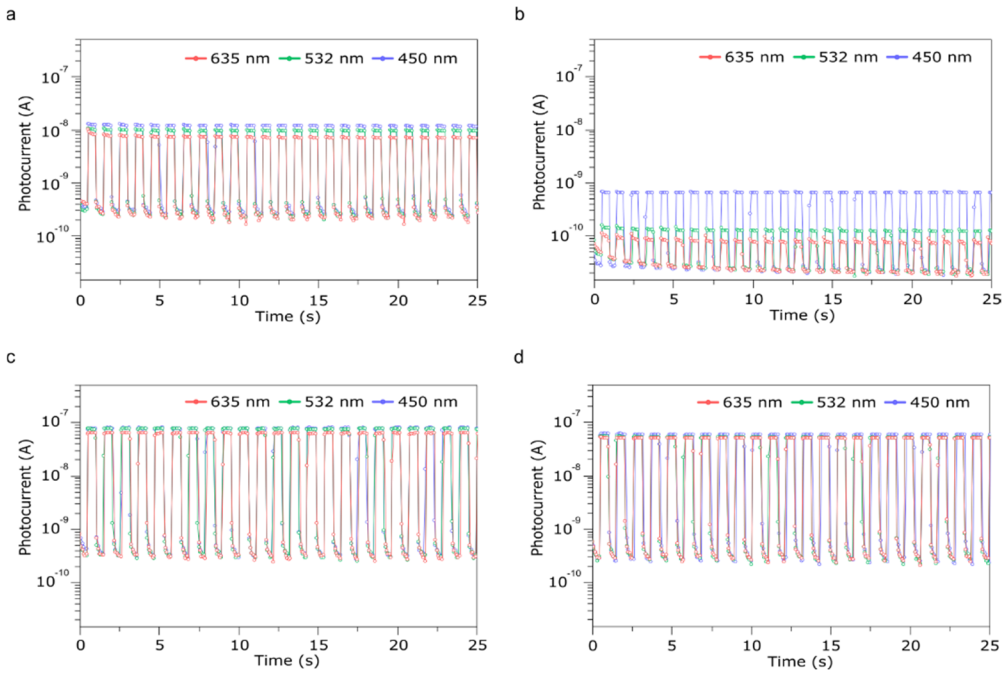

Figure 4. 16 Photocurrent–time responses of the reference γ-$CsPbI_3$ photoresistor at fresh state (a) and after 35 days (b). Photocurrent–time responses of the γ-$CsPbI_3$ (3 wt% OEGDMA) photoresistor at fresh state (d) and after 35 days (e). Photocurrent–time response was measured at 40 V applied bias in the dark and under illumination using the LEDs at 635 nm, 532nm, 450nm with fixed light intensity (P_{in} = 0.4 mW·cm^{-2}) and frequency (1 Hz).

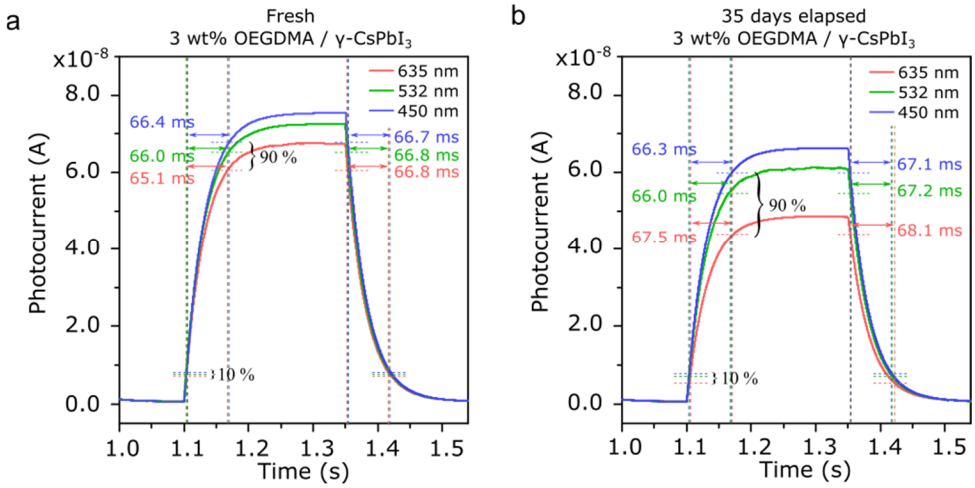

Figure 4. 17 The transient response time of the γ-$CsPbI_3$ (3 wt% OEGDMA) photoresistor at fresh state (a) and after 35 days (b). The transient response time was measured at the 10th period during the 2 Hz, 50% duty cycle with fixed light intensity (P_{in} = 0.4 mW·cm^{-2}).

4.5 Conclusion

In this chapter, I suggest a robust strategy to ensure the structural, electrical long-term stability of γ-$CsPbI_3$ under ambient conditions by employing the infinitesimal amount (≤3 wt%) of UV-curable OEGDMA. The electronegative oxygen lone pairs of the OEGDMA attract Cs^+ and Pb^{2+} cations from the $CsPbI_3$ precursor solution, which induce effective $CsPbI_3$ nucleation and growth from the OEGDMA backbone chain. Additionally, the OEGDMA ($M_n \approx 330$) has short chain lengths with 4 repeating units, resulting in a dense network by the UV-curing, which acts to hold $CsPbI_3$ tightly, thus it is possible to suppress the additional distortion of the γ-$CsPbI_3$ lattice. The OEGDMA polymer network formed by UV irradiation inside the γ-$CsPbI_3$ thin-film clearly contributed to maintaining a considerably stable black phase even when exposed to the ambient conditions for 35 days. To evaluate the electrical long-term stability of the γ-$CsPbI_3$ thin-film employing with the OEGDMA polymer network, 2-terminal lateral photoresistors of Au/γ-$CsPbI_3$ (0, 0.5, 1, 3, and 5 wt% OEGDMA)/Au structure were fabricated, and the photoresistor including optimized UV-cured γ-$CsPbI_3$ (3 wt% OEGDMA) showed that ~90% of the initial electrical values were retained responding to red, green, and blue light even after 35 days in the ambient conditions. Consequently, despite the addition of

a small amount of UV-cured OEGDMA network into the γ-$CsPbI_3$, the γ-$CsPbI_3$'s photoelectric parameters and light response speed remain robust even after prolonged exposure to ambient conditions. Therefore, applying infinitesimal UV-curable polymer network with electronegative lone pair electrons to perovskite is an innovative strategy that can contribute effectively to long-term optical and electrical stability. It also indicates that this strategy can be applied not only to γ-$CsPbI_3$, but also to various halide perovskite materials.

4.6 Experimental details

Preparation of $CsPbI_3$ precursor solution containing a small amount of OEGDMA. The $CsPbI_3$ precursor solution was prepared by dissolving 0.48 M of cesium iodide (CsI, 99.999 %, Sigma Aldrich) and lead iodide (PbI_2, 99 %, Sigma Aldrich) in the mixed solvent of 2 mL of anhydrous N, N-dimethylformamide (DMF, 99.8%) and 72 μL of hydroiodic acid (HI, 57 wt % in H_2O, Sigma Aldrich) and stirred vigorously at 700 rpm over 12 hours [24]. OEGDMA:HMPP mixture with 1 wt% of 2-hydroxy-2-methylpropiophenone (HMPP, 97%, Sigma Aldrich) added to oligo(ethylene glycol) dimethacrylate (OEGDMA, $M_n \approx 330$) as a photoinitiator was added to the prepared $CsPbI_3$ precursor solution as 0, 0.5, 1, 3, 5 wt% of the total amount of CsI and PbI_2. Then stirred vigorously at 700 rpm over 6 hours.

Fabrication process of Au/γ-$CsPbI_3$ (0, 0.5, 1, 3, and 5 wt% OEGDMA)/Au photoresistors. The prepared $CsPbI_3$ precursor solution containing a small amount of OEGDMA was spin-coated on a bare glass substrate in 2 steps. First, the spin-coating was performed at 2000 rpm for 25 seconds, and then spin-coating was immediately performed at 5000 rpm for 35 seconds. After 5 seconds of reaching 5000 rpm, the chlorobenzene was directly dropped on to the substrate to quickly

remove the DMF solvent [35]. After spin-coating process, the $CsPbI_3$ with OEGDMA annealed at 90 °C for 5 minutes and exposed UV for 5 seconds immediately before cooling, which induces to photopolymerization between OEGDMAs. LED UV lamp (365nm, Liim tech) was used as ultraviolet light source. In this study, all UV-curing processes were performed at 400 $mW \cdot cm^{-2}$ for 5 seconds and the distance between the light source and substrate was fixed at 15 mm. Finally, 100 nm gold (Au) electrodes were deposited by the thermal evaporator, with a shadow mask with channel length and width of 120 um, 1000 um, respectively.

Characterizations of optical and photoelectrical properties. The current-voltage characteristics for all devices were measured the voltage range -40V to 40V at room temperature in a dark using the 4155B (Keysight) semiconductor parameter analyzer with the visible light irradiation using LED light sources (STF0A36C, SSC). The optical transmittance and absorbance of the γ-$CsPbI_3$ (0, 0.5, 1, 3, and 5 wt% OEGDMA) films are measured using a UV-VIS spectrometer (PerkinElmer Lambda 35). UV-cured OEGDMA structures are confirmed with attenuated total reflection Fourier transform infrared spectroscopy (ATR-FTIR, BRUKER, Alpha) at 4000-600 cm^{-1} ranges. The crystallinity and morphology of the γ-$CsPbI_3$ (0, 0.5,

1, 3, and 5 wt% OEGDMA) films were obtained using field-emission scanning electron microscopy (FE-SEM, S-4800, Hitachi) and X-ray diffraction (XRD, D8 Advance, Bruker Co.) executed with Cu-Kα radiation (λ = 1.54 Å) at 40 kV and 150 mA (6 kW) with a grazing-incidence mode. X-ray photoelectron spectroscopy (XPS, AXIS SUPRA, Kratos) was used to analyze the chemical properties of the γ-$CsPbI_3$ (0, 0.5, 1, 3, and 5 wt% OEGDMA) films. Time-resolved photoresponse and transient response time were measured by B2902A (Keysight) 2-channel source meter.

4.7 References

[1] Park, N. -K. Organometal perovskite light absorbers toward a 20% efficiency low-cost solid-state mesoscopic solar cell. *J. Phys. Chem. Lett.* **4**, 2423−2429 (2013).

[2] Xing, G. & Nripan, M. et al. Long-range balanced electron and hole-transport lengths in organic-inorganic $CH_3NH_3PbI_3$. *Science* **342**, 344-347 (2013).

[3] Gao, P. et al. Organohalide lead perovskites for photovoltaic applications. *Energy Environ. Sci.* **7**, 2448-2463 (2014).

[4] Hao, F. et al. Lead-free solid-state organic–inorganic halide perovskite solar cells. *Nat. Photonics* **8**, 489-494 (2014).

[5] Dou, L. et al. Solution-processed hybrid perovskite photodetectors with high detectivity. *Nat. Commun.* **5**, 5404 (2014).

[6] Pool, V. L. et al. Thermal engineering of $FAPbI_3$ perovskite material via radiative thermal annealing and in situ XRD. *Nat. Commun.* **8**, 14075 (2017).

[7] Eperon, G. E. et al. Formamidinium lead trihalide: a broadly tunable

perovskite for efficient planar heterojunction solar cells. *Energy Environ. Sci.* **7**, 982-988 (2014).

[8] Xu, L. et al. A comprehensive review of doping in perovskite nanocrystals/quantum dots: evolution of structure, electronics, optics, and light-emitting diodes. *Materials today. Nano* **6**, 100036 (2019).

[9] Bhalla, A. S. et al. The perovskite structure—a review of its role in ceramic science and technology. *Mater. Res. Innov.* **4**, 3-26 (2000).

[10] Conings, B. et al. Intrinsic thermal instability of methylammonium lead trihalide perovskite. *Adv. Energy Mater.* **5**, 1500477 (2015).

[11] Berhe, T. A. et al. Organometal halide perovskite solar cells: degradation and stability. *Energy Environ. Sci.* **9**, 323–356 (2016).

[12] Nam, J. K. et al. Methodologies toward efficient and stable cesium lead halide perovskite-based solar cells. *Adv. Sci.* 1800509 (2018).

[13] Hoffman, J. B. et al. $CsPbBr_3$ solar cells: controlled film growth through layer-by-layer quantum dot deposition. *Chem. Mater.* **29**, 9767−9774 (2017).

[14] Travis, W. et al. On the application of the tolerance factor to inorganic and hybrid halide perovskites: a revised system. *Chem. Sci.* **7**, 4548-4556

(2016).

[15]Sutton, R. J. et al. Bandgap-tunable cesium lead halide perovskites with high thermal stability for efficient solar cells. *Adv. Energy Mater.* **6**, 1502458 (2016).

[16]Liang, J. et al. All-inorganic perovskite solar cells. *J. Am. Chem. Soc.* **138**, 15829−15832 (2016).

[17]Chen, H. et al. Inorganic perovskite solar cells: A rapidly growing field. *Sol. RRL* **2**, 1700188 (2018).

[18]Nam, J. K. et al. Potassium incorporation for enhanced performance and stability of fully inorganic cesium lead halide perovskite solar cells. *Nano Lett.* **17**, 2028−2033 (2017)

[19]Swarnkar, A. et al. Quantum dot–induced phase stabilization of α-$CsPbI_3$ perovskite for high-efficiency photovoltaics. *Science* **354**, 92-95 (2016).

[20]Wang, K. et al. All-inorganic cesium lead iodide perovskite solar cells with stabilized efficiency beyond 15%. *Nat. Commun.* **9**, 4544 (2018).

[21]Marronnier, A. et al. Anharmonicity and disorder in the black phases of cesium lead iodide used for stable inorganic perovskite solar cells. *ACS Nano* **12**, 3477−3486 (2018).

[22]Eperon, G. E et al. Inorganic caesium lead iodide perovskite solar cells. *J. Mater. Chem. A* **3**, 19688 (2015).

[23]Zhao, B. et al. Thermodynamically stable orthorhombic γ-$CsPbI_3$ thin films for high-performance photovoltaics. *J. Am. Chem. Soc.* **140**, 11716−11725 (2018).

[24]Haque, F. et al. Effects of hydroiodic acid concentration on the properties of $CsPbI_3$ perovskite solar cells. *ACS Omega* **3**, 11937−11944 (2018).

[25]Bao, C. et al. High performance and stable all-inorganic metal halide perovskite-based photodetectors for optical communication applications. *Adv. Mater.* **30**, 1803422 (2018).

[26]Jena, A. K. et al. Stabilization of α-$CsPbI_3$ in ambient room temperature conditions by incorporating Eu into $CsPbI_3$. *Chem. Mater.* **30**, 6668−6674 (2018).

[27]Zhang, T. et al. Bication lead iodide 2D perovskite component to stabilize inorganic α-$CsPbI_3$ perovskite phase for high-efficiency solar cells. *Sci. Adv.* **3**, e1700841 (2017).

[28]Hu, Y. et al. Bismuth incorporation stabilized α-$CsPbI_3$ for fully inorganic perovskite solar cells. *ACS Energy Lett.* **2**, 2219−2227 (2017).

[29]Han, B. et al. Stable, efficient red perovskite light-emitting diodes by (α, δ)-$CsPbI_3$ phase engineering. *Adv. Funct. Mater.* **28**, 1804285 (2018).

[30]Li, B. et al. Surface passivation engineering strategy to fully-inorganic cubic $CsPbI_3$ perovskites for high-performance solar cells. *Nat. Commun.* **9**, 1076 (2018).

[31]Wang, Q. et al. Stabilizing the α-phase of $CsPbI_3$ perovskite by sulfobetaine zwitterions in one-step spin coating films. *Joule* **1**, 371–382 (2017).

[32]Jeong, B. et al. All-inorganic $CsPbI_3$ perovskite phase-stabilized by poly(ethylene oxide) for red-light-emitting diodes. *Adv. Funct. Mater.* **28**, 1706401 (2018).

[33]Bäckström, S. et al. Tailoring properties of biocompatible PEG-DMA hydrogels with UV light. *Mater Sci. Appl.* **3**, 425-431 (2012).

[34]Hwang, J. W. et al. Gelation and crosslinking characteristics of photopolymerized poly(ethylene glycol) hydrogels. *J. Appl. Polym. Sci.* **132**, 41939 (2015).

[35]Jeon, N. J. et al. Solvent engineering for high-performance inorganic–organic hybrid perovskite solar cells. *Nat. Mater.* **13**, 897-903 (2014).

Chapter 5 Conclusion

In this thesis, two engineering strategies for securing long-term stability of black phase perovskite under atmospheric conditions were proposed sequentially, and photoelectric properties were evaluated by applying them to phototransistor and photoresistor devices respectively. Chapter 3 introduced the implementation of all-inorganic α-$CsPbI_xBr_{3-x}$, one of the partial substitution methods, that secured long-term stability under atmospheric conditions by introducing the multi anion strategy with low temperature process. Through the electrical and chemical analyses, I found the most stoichiometrically stable $CsPbI_xBr_{3-x}$ film, which was fabricated with 12 wt% additives $CsBr/PbBr_2$ in the $CsPbI_3$ precursor solution. It was confirmed that the stability was maintained by increasing the binding energy while replacing I ions with Br ions, which have a smaller atomic radius, at room temperature. Additionally, phototransistors were fabricated through the heterojunction of $CsPbI_xBr_{3-x}$ and IGZO oxide semiconductor, and the characteristics of the phototransistor were evaluated. The heterojunction phototransistor with $CsPbI_2Br$/IGZO exhibited a responsivity of 26 A/W , a detectivity of 8.42×10^{14} Jones and an external quantum efficiency (EQE) of 51% at the red light power density of 1 mW/cm^2 , which

expanded the detecting range from the ultraviolet to the visible light region. At light irradiation into the heterojunction phototransistor, the excitons photo-generated from $CsPbI_2Br$ were transported along the IGZO back channel, which guaranteed a shorter response time (0.79 s) than that of the conventional IGZO phototransistor. In addition, the heterojunction phototransistor with $CsPbI_2Br$/IGZO showed excellent stability over 1 month under ambient conditions (20 °C, 25% RH).

Furthermore, in Chapter 4, I suggest a robust strategy to ensure the structural, electrical long-term stability of γ-$CsPbI_3$ under ambient conditions through the ultraviolet (UV) curable polyethylene glycol dimethacrylate (OEGDMA) that overcome the bandgap widening issue of partial substitution method. Oxygen lone pair electrons of the OEGDMA capture Cs^+ and Pb^{2+} cations, improving the crystal growth of γ-$CsPbI_3$ around OEGDMA. Additionally, polymer network of OEGDMA processed by UV irradiation, strongly contributes to maintaining the black phase of γ-$CsPbI_3$ structure tight for more than 35 days in ambient conditions. In order to evaluate the optoelectronic properties, two-terminal photoresistors were fabricated in the lateral direction and the effective photocurrent under the visible light was confirmed. The optimized UV-cured 3 wt% OEGDMA/γ-$CsPbI_3$ perovskite film showed that ~90% of the initial electrical properties responding to red, green, and blue light were maintained even after 35 days. These results provide

that introducing the photocurable polymer network is an innovative strategy that can effectively contribute to the long-term stability of the halide perovskite.

Finally, the advantages and disadvantages of my research results and future research directions can be summarized as follows.

■ Advantages

-. The electronegative oxygen lone pairs of the OEGDMA attract Cs^{+} and Pb^{2+} cations from the $CsPbI_3$ precursor solution, which induce effective $CsPbI_3$ nucleation and growth from the OEGDMA backbone chain.

-. Additionally, the OEGDMA ($M_n \approx 330$) has short chain lengths with 4 repeating units, resulting in a dense network by the UV-curing, which acts to hold $CsPbI_3$ tightly, thus it is possible to suppress the additional distortion of the γ-$CsPbI_3$ lattice.

-. Adding a infinitesimal amount (≤ 3 wt%) of UV-cured OEGDMA polymer network ensures long-term photoelectrical and optical stability under atmospheric conditions without deterioration of $CsPbI_3$'s electrical properties.

■ Disadvantages

-. Although UV exposure is a very simple process, this strategy can increase the

overall cost of the process as UV-curing step is added in terms of the process.

-. Since this study is for ensuring long-term stability of $CsPbI_3$ containing Pb ions, it is not basically an eco-friendly inorganic perovskite that is Pb free.

■ Future research direction

-. Extended research is needed to see if the addition of UV-cured OEGDMA polymer network can also help the long-term stability of various inorganic perovskites.

-. Evaluate whether it contributes to long-term stability under the atmospheric conditions of perovskite when applied with other UV-curable polymer network with electronegative lone pair electrons as well as OEGDMA.

List of publications

-. **Nam-Kwang Cho**‡, Jinil Cho‡, Gayeong Yoo, Jae-eun Huh, Suyeon Lee, Sunghee Kim, Soo-Young Yoon, Jeeyoung Yoo*, and Youn Sang Kim*, "Mobility Boost Up of Hybrid TFT with Solvent-Free Cross-Linked Polyurethane-Ionic Liquid Gate Dielectric" *Appl. Phys. Express* **12**, 101004 (2019)

-. **Nam-Kwang Cho**‡, Jintaek Park‡, Donggun Lee, Jun-Woo Park, Won Hyung Lee, and Youn Sang Kim*, "Investigation of Vertical Current Phenomena in the Insulator/Oxide Semiconductor Heterojunction Using XPS Analysis and an Atmospheric-Pressure Plasma Treatment System" *ACS Appl. Electron. Mater.* **1**, 1698−1704 (2019)

-. Hyun-Jae Na‡, **Nam-Kwang Cho**‡, Jintaek Park, Sung-Eun Lee, Eun Goo Lee, Changik Im and Youn Sang Kim*, "A Visible Light Detector Based on a Heterojunction Phototransistor with a Highly Stable Inorganic CsPbIxBr3-x Perovskite and In–Ga–Zn–O Semiconductor Double-layer" *J. Mater. Chem. C* **7**, 14223-14231 (2019)

-. Jintaek Park‡, **Nam-Kwang Cho**‡, Sung-Eun Lee, Eun Goo Lee, Junhee Lee , Changik Im , Hyun-Jae Na and Youn Sang Kim*, "Atmospheric-Pressure Plasma Treatment Toward High-Quality Solution-Processed Aluminum Oxide Gate Dielectric Films in Thin-Film Transistors" *Nanotechnology* **30**, 195702 (2019)

-. Sungho Park‡, **Nam-Kwang Cho**‡, Byung Jun Kim, Shin Young Jeong, Il Ki Han, Youn Sang Kim, and Seong Jun Kang*, "Reducing the Persistent Photoconductivity Effect in Zinc Oxide by Sequential Surface Ultraviolet Ozone and Annealing Treatments" *ACS Appl. Electron. Mater.* **1**, 2655−2663 (2019)

-. Byung Jun Kim‡, **Nam-Kwang Cho**‡, Sungho Park, Shinyoung Jeong, Dohyeon Jeon, Yebin Kang, Taekyeong Kim, Youn Sang Kim, Il Ki Han and Seong Jun Kang*, "Highly Transparent Phototransistor Based on Quantum-Dots and ZnO Bilayers for Optical Logic Gate Operation in Visible-Light" *RSC Adv.* **10**, 16404-16414 (2019)

-. **Nam-Kwang Cho**, Sang Moo Lee, Kigook Song and Seong Jun Kang*, "Enhanced Quantum-dot Light-Emitting Diodes Using Gold Nanorods" *J. Korean Phys. Soc.* **67**, 1667-1671 (2015)

-. Donggun Lee, Jun-Woo Park, **Nam-Kwang Cho**, Jinwon Lee and Youn Sang Kim*, “Verifcation of Charge Transfer in Metal-Insulator-Oxide Semiconductor Diodes via Defect Engineering of Insulator” *Sci. Rep.* **9**, 10323 (2019)

-. Jun-Woo Park, Donggun Lee, **Nam-Kwang Cho**, Jinwon Lee*, and Youn Sang Kim*, ”Turn-On Voltage Shift of Metal−Insulator−Oxide Semiconductor Thin-Film Diode by Adding Schottky Diode in Reverse Direction” *ACS Appl. Electron. Mater.* **1**, 530−537 (2019)

-. Sung-Eun Lee, Jintaek Park, Junhee Lee, Eun Goo Lee, Changik Im, Hyunjae Na, **Nam-Kwang Cho**, Keon-Hee Lim* and Youn Sang Kim*, “Surface-Functionalized Interfacial Self-Assembled Monolayers as Copper Electrode Diffusion Barriers for Oxide Semiconductor Thin-Film Transistor” *ACS Appl. Electron. Mater.* **1**, 430−436 (2019)

-. Jong-Baek Seon, **Nam-Kwang Cho**, Gayeong Yoo, Youn Sang Kim* and Kookheon Char*, “Solution-Processed Amorphous ZrO_2 Gate Dielectric Films Synthesized by a Non-Hydrolytic Sol–Gel Route” *RSC Adv.* **8**, 39115–39119 (2018)

-. Jinwon Lee, Kapsoo Yoon, Keon-Hee Lim, Jun-Woo Park, Donggun Lee, **Nam-Kwang Cho** and Youn Sang Kim*, “Vertical Transport Control of Electrical Charge Carriers in Insulator/Oxide Semiconductor Hetero-structure” *Sci. Rep.* **8**, 5643 (2018)

-. Sungho Park, Byung Jun Kim, **Nam-Kwang Cho** and Seong Jun Kang*, “Photocurrent Characteristics of Zinc-Oxide Films Prepared by Using Sputtering and Spin-Coating Methods” *J. Korean Phys. Soc.* **73**, 1351-1355 (2018)

-. Bu-il Nam, Jong Seo Park, Keon-Hee Lim, Yong-keon Ahn, Jinwon Lee, Jun-woo Park, **Nam-Kwang Cho**, Donggun Lee, Han-Bo-Ram Lee* and Youn Sang Kim*, “Conduction Mechanism Change with Transport Oxide Layer Thickness in Oxide Hetero-Interface Diode” *Appl. Phys. Lett.* **111**, 053506 (2017)

-. Keon-Hee Lim, Jae-Eun Huh, Jinwon Lee, **Nam-Kwang Cho**, Jun-woo Park, Bu-il Nam, Eungkyu Lee and Youn Sang Kim*, “Strong Influence of Humidity on Low-Temperature Thin-Film Fabrication via Metal Aqua Complex for High Performance Oxide Semiconductor Thin-Film Transistors” *ACS Appl. Mater.*

Interfaces **9**, 548−557 (2017)

-. Sang Moo Lee, Dongguen Shin, **Nam-Kwang Cho**, Yeonjin Yi and Seong Jun Kang*, “A Solution-Processable Inorganic Hole Injection Layer that Improves the Performance of Quantum-Dot Light-Emitting Diodes” *Curr. Appl. Phys.* **17**, 442-447 (2017)

-. Jongwon Choi, Junghak Park, Keon-Hee Lim, **Nam-Kwang Cho**, Jinwon Lee, Sanghun Jeon* and Youn Sang Kim*, “Photosensitivity of InZnO Thin-Film Transistors Using a Solution Process” *Appl. Phys. Lett.* **109**, 132105 (2016)

-. Sang Moo Lee, **Nam-Kwang Cho**, and Seong Jun Kang*, “Quantum-Dot Light-Emitting Diodes with a Double-Layer Structured Hole Injection Layer” *J. Vac. Sci. Technol. B.* **33**, 062401 (2015)

요 약 (국문초록)

흑색 상 무기 $CsPbI_3$ 페로브스카이트의 장기 안정성 향상 공정개발에 관한 연구

조 남 광
융합과학부 나노융합전공
융합과학기술대학원
서울대학교

할라이드 페로브스카이트는 높은 흡광계수와 긴 엑시톤 확산길이 및 밴드갭을 조절 가능한 특징들로 인하여 태양전지 및 광 검출기 분야에서 차세대 광 흡수제로써 상당한 관심을 끌었다. 이러한 할라이드 페로브스카이트에 대한 연구는, 최근에는 가시광 영역 전체에 걸쳐 우수한 흡광 특성을 갖는 좁은 밴드갭 (~1.72 ev)의 흑색 (α, γ 상) 할라이드 페로브스카이트 구현에 초점이 맞추어져 왔으며, 이와 더불어 대기 조건 하에서 흑색 상의 장기안정성을 확보하기 위한 연구가 집중적으로 수행되었다.

그럼에도 불구하고 페로브스카이트를 대기 조건 하에서 장기적으로 흑색 상을 유지시키기 위한 공정 방법론적인 문제는 여전히 남아있으며 추가적인 개선의 여지가 분명히 존재한다.

본 논문에서는 대기 조건 하에서 흑색 상 페로브스카이트의 장기 안정성을 확보하기 위한 두 가지 공정 전략을 순차적으로 제안하였으며, 이 전략들을 포토트랜지스터 및 포토레지스터 소자에 각각 적용하여 광전기적 특성을 평가하였다. 먼저, 브롬 이온을 요오드 위치에 부분적으로 치환시킨 α-$CsPbI_xBr_{3-x}$를 저온공정을 통하여 대기중에서 안정적으로 흑색 상을 유지할 수 있는 방법을 제안하였다. 이 방법을 통하여 제작한 α-$CsPbI_xBr_{3-x}$를 IGZO 산화물 반도체와 이종 접합시킴으로써 포토트랜지스터를 제작하였고 광전기적 특성을 평가하였다. 또한, 이 연구를 통하여 α-$CsPbI_xBr_{3-x}$/IGZO 이종접합이 IGZO 본래의 photoillumination stress를 크게 완화시키는 것을 확인하였다.

그러나, 요오드 위치에 부분적으로 브롬 이온을 치환시키게 되면, 밴드갭이 $CsPbI_3$ 고유의 밴드갭 보다 넓어지는 근본적인 한계점을 내포하고 있으므로, 이러한 문제를 극복하기 위하여 자외선 경화가능한 폴리에틸렌 글리콜 디 메타크릴레이트 (PEGDMA)를 도입하여 대기 조건 하에서 γ-CsPbI3의 구조적, 전기적 장기 안정성을 보장하는 강력한 전략을 추가적으로 제안하였다. PEGDMA 내부에 존재하는 다량의 산소 고립전자쌍들

이 세슘 및 납 양이온들을 포획하여 PEGDMA 주위에서부터 γ-$CsPbI_3$의 결정 성장을 유도하였으며, 추가적으로 자외선 경화를 통해 PEGDMA 네트워크가 γ-$CsPbI_3$구조를 단단하게 고정시켜 줄 수 있도록 하였다. 또한, 2 단자 포토레지스터 소자를 구현하여 가시광 조사 시, 유효한 광전류를 35일간 대기중에서 노출되어도 90%이상 유지됨을 확인하였다. 이러한 결과들은 광 경화성 고분자 네트워크를 적용한 공정방법이 할라이드 페로브스카이트의 장기안정성에 효과적이고 범용적으로 기여할 수 있는 혁신적인 전략이 될 수 있음을 시사한다.

주요어: 장기 안정성, γ-$CsPbI_3$, 무기 할라이드 페로브스카이트, 흑색 상, 자외선 경화성 고분자 네트워크, 포토레지스터

학 번: 2015-30720